

Copyright Warning & Restrictions

The copyright law of the United States (Title 17, United States Code) governs the making of photocopies or other reproductions of copyrighted material.

Under certain conditions specified in the law, libraries and archives are authorized to furnish a photocopy or other reproduction. One of these specified conditions is that the photocopy or reproduction is not to be “used for any purpose other than private study, scholarship, or research.” If a user makes a request for, or later uses, a photocopy or reproduction for purposes in excess of “fair use” that user may be liable for copyright infringement,

This institution reserves the right to refuse to accept a copying order if, in its judgment, fulfillment of the order would involve violation of copyright law.

Please Note: The author retains the copyright while the New Jersey Institute of Technology reserves the right to distribute this thesis or dissertation

Printing note: If you do not wish to print this page, then select “Pages from: first page # to: last page #” on the print dialog screen

The Van Houten library has removed some of the personal information and all signatures from the approval page and biographical sketches of theses and dissertations in order to protect the identity of NJIT graduates and faculty.

ABSTRACT

III-NITRIDE ULTRAVIOLET LIGHT-EMITTING DIODES: APPROACHES FOR THE ENHANCED EFFICIENCY

by
Moulik Patel

III-nitride ultraviolet (UV) light-emitting diodes (LEDs) offer marvelous potential for a wide range of applications, including air/water purification, surface disinfection, biochemical sensing, cancer cell elimination, and many more. III-nitride semiconductor alloys, especially AlGa_N and AlIn_N, have drawn significant attention due to their significant advantages that include environmental-friendly material composition, compact in size, longer lifetime, low power consumption, and tunable optical emission. However, the performance of III-nitride UV LEDs in terms of efficiency and output power is still deficient. The presence of high defects and dislocations due to lattice-mismatched epilayers, polarization induced quantum-confined Stark effect, electron overflow with low hole injection efficiency is found to be some of the primary reasons behind it. In this thesis, we have investigated in a concave quantum barrier structure approach for the enhanced device performance of AlGa_N UV LEDs. The proposed concave quantum barriers could suppress the electron leakage by significantly reducing the electron mean free path that improves the electron capturing capability in the active region. The proposed structure exhibits an optical power of 9.16 mW at ~284 nm wavelength, which is increased by ~40.5% compared to conventional AlGa_N UV LED operating at 60 mA injection current. Additionally, the light extraction efficiency of AlIn_N nanowire UV LEDs has been studied. The results show that the TM-polarized light extraction efficiency of such UV LED without any passivation is only ~25.2%, whereas the maximum recorded light extraction efficiency

is ~40.6% with the utilization of 40 nm HfO₂ passivation layer. This study provides a promising approach for enhancing the light extraction efficiency of nanowire UV LEDs.

**III-NITRIDE ULTRAVIOLET LIGHT-EMITTING DIODES: APPROACHES
FOR THE ENHANCED EFFICIENCY**

**by
Moulik Patel**

**A Thesis
Submitted to the Faculty of
New Jersey Institute of Technology
in Partial Fulfillment of the Requirements for the Degree of
Master of Science in Engineering Science**

Newark College of Engineering

May 2021

Blank Page

APPROVAL PAGE

**III-NITRIDE ULTRAVIOLET LIGHT-EMITTING DIODES: APPROACHES
FOR THE ENHANCED EFFICIENCY**

Moulik Patel

Dr. Hieu Pham Trung Nguyen, Thesis Advisor Date
Associate Professor of Electrical and Computer Engineering, NJIT.

Dr. Dong-Kyun Ko, Committee Member Date
Associate Professor of Electrical and Computer Engineering, NJIT.

Dr. Xuan Liu, Committee Member Date
Associate Professor of Electrical and Computer Engineering, NJIT.

BIOGRAPHICAL SKETCH

Author: Moulik Patel

Degree: Master of Science

Date: May 2021

Undergraduate and Graduate Education:

- Master's in Engineering Science
New Jersey Institute of Technology, Newark, NJ, 2021
- Bachelor of Science
K.J. Somaiya College of Engineering, Mumbai, India, 2016

Major: Engineering Science

Presentations and Publications:

Peer Reviewed Papers

- M. Patel**, B. Jain, R. T. Velpula, and H. P. T. Nguyen, "Effect of HfO₂ Passivation Layer on Light Extraction Efficiency of AlInN Nanowire Ultraviolet Light-Emitting Diodes." *ECS Transaction*, In Press.
- B. Jain, R. T. Velpula, **M. Patel**, and H. P. T. Nguyen, "Controlled carrier mean free path for the enhanced efficiency of III-nitride deep-ultraviolet light-emitting diodes," *Applied Optics*, 60, 3088-3093 (2021).
- B. Jain, R.T Velpula. **M. Patel**, S.M. Sadaf, H.P.T. Nguyen, "Improved Performance of Electron Blocking Layer Free AlGaN Deep Ultraviolet Light-Emitting Diodes Using Graded Staircase Barriers", *Micromachines*, 12, 334 (2021).
- B. Jain, R. T. Velpula, **M. Patel**, and H. P.T. Nguyen. "High performance electron blocking layer free ultraviolet light-emitting diodes." In *Physics and Simulation of Optoelectronic Devices XXIX*, International Society for Optics and Photonics, 11680, 1168012. 2021.

Conferences

M. Patel, B. Jain, R.T. Velpula, and H. P. T. Nguyen, "Effect of HfO₂ Passivation Layer on Light Extraction Efficiency of AlInN Nanowire Ultraviolet Light-Emitting Diodes.", *239th ECS Meeting with the 18th International Meeting on Chemical Sensors (IMCS) (May 30-June3, 2021)*. ECS, 2021.

B. Jain, R.T. Velpula, H.Q. Bui, **M. Patel**, and H.P.T. Nguyen, "Electron Blocking Layer Free Full-Color InGaN/GaN White Light-Emitting Diodes. *238th ECS Meeting with the 17th International Meeting on Chemical Sensors (IMCS)*. ECS, 2020.

ACKNOWLEDGMENT

This study would not be possible without the help of professor Dr. Hieu Pham Trung Nguyen. I have thoroughly enjoyed learning under his advisement. His passion for research and openness to new ideas has inspired me.

I would like to thank the members in my research group Ravi Teja Velpula, Barsha Jain and Victor Bui. They were my support system, teachers, friends and really helped my transition into research from engineering.

The department of Electrical and Computer Engineering at New Jersey Institute of Technology and its administration run by, Tanita, Barbara, Monteria, and Joan, who help run it so smoothly were of great help.

Finally, I would like to thank Dr. Edwin Hou, my academic adviser, for telling me about this opportunity, thus making this master's program a worthwhile one, thank you.

TABLE OF CONTENTS

Chapter		Page
1	INTRODUCTION.....	1
	1.1 Motivation.....	1
	1.2 Light Emitting Diode.....	3
	1.3 Materials for UV-LED.....	4
	1.4 Simulation Tools.....	6
	1.4.1 Advanced Physical Models of Semiconductor Devices (APSYS).....	6
	1.4.2 Finite difference Time domain with Lumerical.....	10
	1.5 Thesis Overview.....	12
2	FACTORS AFFECTING INTERNAL QUANTUM EFFICIENCY AND EFFICIENCY DROOP.....	14
	2.1 Radiative Recombination.....	14
	2.2 Non-Radiative Recombination.....	15
	2.2.1 Auger Recombination.....	15
	2.2.2 SRH Recombination.....	16
	2.2.3 Surface Recombination.....	19
	2.3 Electron Overflow.....	20
	2.4 Simulation Setup.....	21
	2.5 Results and Discussion.....	22
3	MITIGATING THE ELECTRON LEAKAGE IN ALGAN DEEP UV LEDS USING CONCAVE QUANTUM BARRIER STRUCTURE.....	28
	3.1 Introduction.....	28

TABLE OF CONTENTS
(continued)

Chapter		Page
	3.2 Simulation and Structural Parameters.....	28
	3.3 Results.....	31
4	IMPROVING THE LIGHT EXTRACTION EFFICIENCY OF ALINN NANOWIRE ULTRAVIOLET LIGHT-EMITTING DIODES BY HFO ₂ SURFACE PASSIVATION.....	40
	4.1 Introduction	40
	4.2 Simulation Setup.....	41
	4.3 Results.....	43
5	CONCLUSION AND FUTURE WORK.....	50
	5.1 Study of Doping and Defects in AlInN UV LEDs.....	50
	5.2 Study of Photonic Crystal Structure for AlInN UV nanowire LEDs	53

LIST OF FIGURES

Figure	Page
1.1 Early design in LEDs using Homojunction Method.....	3
1.2 Wurtzite Cell Structure.....	5
1.3 General Workflow for a TCAD Simulation	9
1.4 Snapshot of Lumerical Layout for the Purpose of Design and Simulation for Different Parts.....	12
2.1 Illustration of Simplified Light-Matter Interaction.....	15
2.2 Illustration of Different Recombination Processes.....	18
2.3 Schematic Diagram of the Simulated AlGaIn UV LED at 255nm.....	22
2.4 Plots for Hole Concentration in a Quantum Well for 1 Quantum Well and 2 Quantum Well Design.....	25
2.5 Plots for Hole Concentration in a Quantum Well for 3-6 Quantum Well Design.....	25
2.6 Plots for Hole Concentration in a Quantum Well for 7-8 Quantum Well Design.....	26
2.7 Plots for Power vs Current and IQE vs Current for 1- 4 Quantum Well Design.....	26
2.8 Plots for Power vs Current and IQE vs Current for 5- 8 Quantum Well Design.....	27
3.1 Schematic Representation of LED with Al Composition Profile Related to the Conduction Band of Conventional Structure and Proposed Structure.....	29
3.2 Energy Band Diagram of a Conventional LED and a Proposed LED at 60 mA Current Injection.....	31
3.3 Schematic of Energy Band Diagram of a Conventional LED and a Proposed LED with Electrostatic Field in MQWs of said LEDs.....	33

LIST OF FIGURES
(continued)

Figure	Page
3.4 Electron Concentration, Electron Leakage, Hole Concentration, and Radiative Recombination Rate in MQWs of a Conventional LED and Proposed LED.....	37
3.5 Calculated IQE, EL Intensity, Power and Voltage Characteristics of Conventional LED and Proposed LED as a Function of Injection Current.....	38
3.6 IQE at 60 mA, IQE Droop During 0-60 mA Current Injection and Output Power at 60 mA for Different LED Designs.....	39
4.1 Schematic Illustration of AlInN-based NW UV LED with HfO ₂ Passivation Layer and a Cross-Sectional View of NW from the Top.....	42
4.2 Schematic Illustration of AlInN-based Planar UV LED with TM Polarized Light Source.....	43
4.3 Cross-Sectional Near-Field Electric Field Intensity of a TE & TM-Polarized Light Source for AlInN NW LED.....	44
4.4 The LEE of the AlInN NW LED as a Function of Wavelength.....	45
4.5 TE-Polarized, TM-Polarized LEE of the AlInN NW LED as a Function of HfO ₂ Passivation Layer Thickness.....	46
4.6 Electric Field Profile for a TM-Polarized Light Source for a AlInN NW Core in the X-Y Plane for a 40 nm Thick HfO ₂ Passivation Layer and a 75 nm Thick HfO ₂ Passivation Layer.....	47
4.7 Cross-Sectional Absorption Profile in the X-Y Plane for a 40 nm Thick Passivation Layer and a 75 nm Passivation Layer.....	48
4.8 Cross-Sectional Near-Field Electric Field Intensity of a TM-Polarized Light Source for AlInN NW LED Without Passivation Layer, with a 40 nm and a 75 nm Passivation Layer for TM-Polarized Light Source in the X-Y Plane.....	49
5.1 Doped GaN and its Effect on Density of state for GaN Material.....	52
5.2 Example for Photonic Crystal Structure of an AlInN NW UV-LED.....	54

LIST OF TABLES

Table	Page
1.1 Classification of the Ultraviolet Light with Respect to Wavelength Range.....	1
1.2 Comparing Electrical and Optical Efficiency of Different UV Light Sources.....	2
2.1 Results Presenting Peak Radiative Recombination Values for Each Well with Varying Number of Quantum Wells.....	23
2.2 Results Presenting Peak Auger Recombination Values for Each Well with Varying Number of Quantum Wells.....	24
2.3 Results Presenting Peak SRH Recombination Values for Each Well with Varying Number of Quantum Wells.....	24
3.1 Effective Conduction Band Barrier Heights of Quantum Barriers and EBL for Conventional LED and Proposed LED.....	32
3.2 Effective Valence Band Barrier Heights of Quantum Barriers and EBL for Conventional LED and Proposed LED.....	32

CHAPTER 1

INTRODUCTION

1.1 Motivation

Ultraviolet (UV) radiation constitutes about $1/10^{\text{th}}$ of the total electromagnetic radiation output from the Sun. Discovered in 1801, by German physicist Johann Wilhelm Ritter, who observed that invisible rays just beyond the violet end of the visible spectrum darkened silver chloride-soaked paper more quickly than violet light itself, calling them (de-) oxidizing rays to emphasize chemical reactivity. The UV spectrum is classified using wavelength range as the following Table 1.1 [1]:

Table 1.1 Classification of the Ultraviolet Light with Respect to Wavelength Range.

Name	Abbreviation	Wavelength Range
Ultraviolet-A	UV-A	400 nm-315 nm
Ultraviolet-B	UV-B	315 nm-280 nm
Ultraviolet-C	UV-C	280 nm-200 nm

Physicist Victor Schumann discovered ultraviolet radiation with wavelengths below 200 nm and named them vacuum UV, since the oxygen in the atmosphere strongly absorbs these radiations [2]. UV LEDs have seen tremendous growth over the past several years. This is not only the result of technological advances in the manufacturing of solid-state UV devices, but the ever-increasing demand for environmentally friendly methods of producing UV light which is currently dominated by mercury lamps. A continuous low-pressure mercury (LPM) lamp that emits continuous radiation in a narrow UV spectrum. Because it uses mercury, this process leads to an environmental concern [3]. Also, mercury

vapor lamps are effective for continuous operation environment since it requires a warmup and cool-down period which increases energy consumption and time whereas pulse xenon lamp can be switched. Increased risk of damage to the primary products and other materials exposed to this light is possible with continuous use.

A pulse xenon lamp (PXL), emitting a high-power pulse of radiation in UV, visible and near-infrared regions, is a gas discharge lamp. Xenon, a benign gas, has broader antimicrobial action compared with the other UV LEDs. The efficiency and intensity of the Low-Pressure Mercury lamps are lower than the Xenon lamp. But these Xenon lamps require a special hardware to operate to ensure compressed high-power radiation to ensure robust antimicrobial function. With these considerations LEDs are compact, with long working life, with an option for pulsed operation, and an ease with which they can be integrated with electronics. However, UV LED efficiency is low, but it can be improved if we learn the mechanism of their operation and apply certain design techniques, thus improving them. Table 1.2 shows the comparison of Electrical and Optical efficiency of the above-mentioned commercial light source method with the LED.

Table 1.2 Comparing Electrical and Optical Efficiency of different UV light sources.

Source	Electrical efficiency (%)	optical efficiency (%)
LPM	50	38
PXL	15-20	17
UV-LED	60	10

Source: Schaefer, Raymond & Grapperhaus, Michael & Schaefer, Ian & Linden, Karl. (2007). Pulsed UV lamp performance and comparison with UV mercury lamps. *Journal of Environmental Engineering and Science - J ENVIRON ENG SCI.* 6. 303-310

1.2 Light Emitting Diodes

Extrinsic semiconductors are generally used for light-emitting applications. In an intrinsic semiconductor holes in the valence band are vacancies created by electrons that have been thermally excited to the conduction band. While extrinsic semiconductors are doped i.e., impurities are added to intrinsic semiconductors.

Doped semiconductors are where holes or electrons are supplied by a foreign atom acting as an impurity. Furthermore, the extrinsic semiconductor can be further classified as *p*-type or *n*-type depending on the impurity atom type added. A *p*-type semiconductor is an intrinsic semiconductor (like Si) in which an impurity acting as an acceptor (like e.g., boron B in Si) has been intentionally added. These impurities are called acceptors since once they are inserted in the crystalline lattice, they lack one or several electrons (designated as holes) to realize a full bonding with the rest of the crystal. In contrast, *n*-type semiconductors have impurities that donate their electrons to the bulk system.

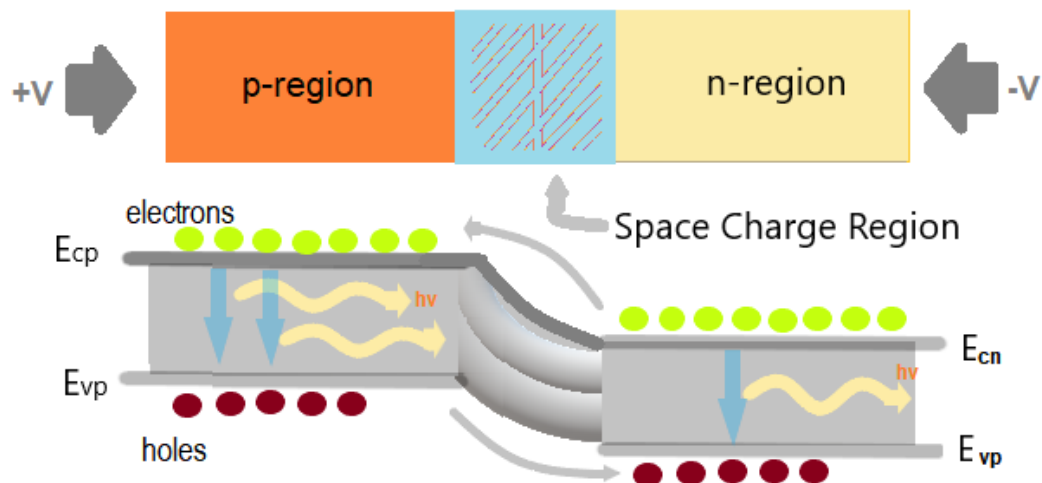


Figure 1.1 Early Design of an LED using Homojunction Method.

When a potential is applied across this junction to make it forward bias, current flows as in the case of any *p-n* junction. The electrons from the *n*-type region are pushed towards the

p-region and thus enter the junction while holes from the *p*-type region are pushed into the junction, which recombine like a normal diode to enable the current to flow. When this occurs the recombination releases energy some of this is in the form of photons this can be visualized in Figure 1.1.

But this Homojunction structure design has some inherent problems, mainly with the requirement of narrow *p*-region and higher re-absorption chance due to high material volume requirement. So, heterojunction Quantum structure design is favored due to its increased carrier injection efficiency by using the quantum well (QW) structure and use of wide-bandgap quantum barriers are transparent to the photons generated in the narrow-bandgap QW layers results in reduced photon re-absorption.

1.3 Materials for UV-LED

Alloying among the group-III nitrides allows one to engineer the band gap from 0.70 eV (InN) to 6.28 eV (AlN) with an intermediate value of 3.44 eV (GaN). Ternary alloys like InGaN, AlGaN, and AlInN enables the fabrication of LEDs and laser diodes operating in the IR to UV spectral region. Wurtzite group III-nitrides, including binaries (GaN, InN, and AlN), ternary ($\text{In}_x\text{Ga}_{1-x}\text{N}$, $\text{Al}_y\text{Ga}_{1-y}\text{N}$ and $\text{Al}_z\text{In}_{1-z}\text{N}$) and quaternary ($\text{In}_p\text{Al}_q\text{Ga}_{1-p-q}\text{N}$) alloys, are considered to be one of the most important semiconductor materials of today. The direct bandgap across all compositions and the wide bandgap range achievable with these III-nitrides alloys. InGaN is used for visible LEDs since its bandgap energy is in this wavelength range. To achieve short wavelength emission, usually aluminum mole fraction is required for III-nitride system. Thus, the materials considered for this study will be AlGaN and AlInN. Nitride semiconductors and their alloys can crystallize in three structures namely the hexagonal wurtzite phase, the cubic zincblende phase and the rock-

salt phase. Not only the wurtzite phase is thermodynamically stable, but also zincblende structure can be obtained using epitaxial growth on an oriented cubic surface. The wurtzite structure can be described as two interpenetrating hexagonally close-packed (hcp) sublattices shifted along c axis. Additionally, wurtzite structure is characterized by an internal parameter u , defined such a way that the anion-cation bond length along the (0001) axis is cu . The lattice parameters a and b are the length of the sides as shown, while the lattice parameter c is the height of the unit cell as shown in Figure 1.2.

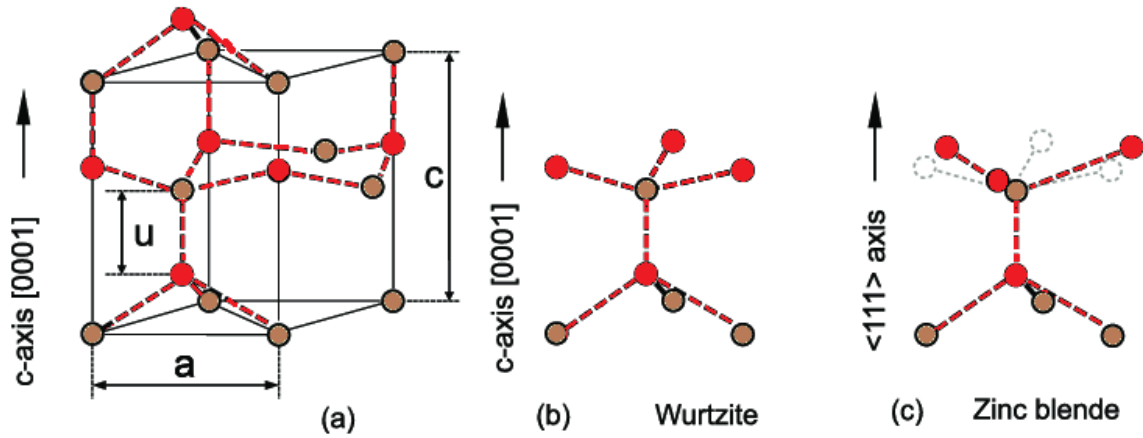


Figure 1.2 Illustration of a Wurtzite cell Structure shown in (a) Atomic Placing of Involved III-N Elements in Wurtzite Structure is shown in (b) Relative Placing of Atoms in Zinc Blende Structure is shown in (c).

The group III-nitrides have polar axes due to a lack of inversion symmetry. In particular, the bonds in the $\langle 0001 \rangle$ direction for wurtzite and $\langle 111 \rangle$ direction for zincblende are all faced by nitrogen in the same direction and by the cation (Al, Ga or In) in the opposite. For example, in the GaN structure, Ga-faced conventionally means Ga on the top position of the $[0001]$ bilayer, corresponding to $[0001]$ polarity. Each III-N bond is partly ionic [4] and the electrons are pulled more towards N atom is due to the large electronegativity difference between the two atoms. Hence, a dipole moment is formed at each III-N bond. The non-centrosymmetric wurtzite structure means these dipole moments cannot be

cancelled as found in other symmetric zinc-blende structures and this net polarization known as the spontaneous polarization. Piezoelectric polarization is induced due to the lattice mismatch between epi-layers and can be found in strained III-nitride materials.

The simplest possible prediction of a physical property for example, bandgap of the above-mentioned ternary III-nitride semiconductor alloy, is to assume it changes linearly between the values at its endpoints corresponding to the relevant binary compounds. This is generally considered to be valid in the case of lattice constant variation with composition and is expressed using Vegard's law. For most semiconductor materials, the bandgap of an alloy does not follow a linear Vegard's law [eq 1.1] with composition; and some degree of deviation is typically observed. This is commonly accounted for through the inclusion of a so-called "bowing parameter" b , (eq 1.2) leading to a parabolic dependence.

$$a_{A(1-x)Bx} = (1 - x) * a_A + x * a_B \quad (1.1)$$

$$E_{g(AlGaN)} = xE_{g,AlN} + (1 - x)E_{g,GaN} - bx(1 - x) \quad (1.2)$$

1.4 Simulation Tools

1.4.1 Advanced Physical Models of Semiconductor Devices (APSYS)

The unique thermal, optical, and electrical characteristics of LEDs such as the band diagram, carrier distribution, carrier current density, electrostatic field, radiative/non-radiative recombination rates, TE/TM radiative recombination rates, internal quantum efficiency (IQE), current-voltage (I-V), and output power-current (L-I) characteristics etc. can be studied using Crosslight Advanced Physical Models of Semiconductor Devices (APSYS) simulation software. The APSYS uses 2D/3D finite element analysis of electrical, optical, and thermal properties of silicon and compound semiconductor devices

and solves the poisson's equation, the current continuity equation, the carrier energy transport equation, quantum mechanical wave equations, and the scalar wave equations for the photonic devices. The popular drift-diffusion current equations can be derived from the Boltzmann transport equation (BTE) by considering its moments and is generally used for modelling a flow in a semiconductor. The BTE is given as

$$\partial_t f + v(k) \cdot \nabla_x f + (q/h) \nabla_x V \cdot \nabla_k f = Q(f) \quad (1.3)$$

This equation is obtained from considering a semi-classical picture of an electron in semiconductor.

$$\partial_t x = \nabla_k E(k) \quad (1.4)$$

$$\dot{k} = q \nabla_x V(x) \quad (1.5)$$

$$p = m^* v \quad (1.6)$$

Additionally,

$$\varepsilon_s \Delta V = -\varepsilon_s \text{div}(E_{mean} + E_{ext}) = q(n - C(x)) \quad (1.7)$$

is the Poisson equation where E_{ext} is the external potential and $C(x)$ is the doping profile and m^* is the effective mass in equation 1.6.

The zeroth-order moment of the above BTE gives continuity equation an example given below in equation 1.7, which is the lowest order moment obtained by integrating, while the first moment gives a drift-diffusion equation leads to drift diffusion current equation shown in equation 1.10 and 1.11.

$$\frac{\partial n}{\partial t} - \frac{1}{q} \nabla_r J + R = G \quad (1.8)$$

Generally, the semi-classical Boltzmann equation is greater than 3-dimensional so numerical simulations extremely time-consuming. Further, only macroscopic physical variables (particle density n , velocity v , energy e) are of interest and can be calculated using equation (1.9).

$$(n, v, e) = \int_{R^3} f(k) \left(1, k, \frac{1}{2} |k|^2 \right) \frac{dk}{4\pi^3} \quad (1.9)$$

usually evaluating equations by integrating Boltzmann equation over k over a Brillouin zone. The drift diffusion current equations are obtained from first moment of BTE and it is widely used in semiconductor modelling is shown in equations 1.9 and 1.10.

$$J_n = qn(x)\mu_n E(x) + qD_n \frac{dn}{dx} \quad (1.10)$$

$$J_p = qn(x)\mu_p E(x) - qD_p \frac{dn}{dx} \quad (1.11)$$

A numerical scheme which solves these continuity equations must

- Conserve the total charge inside the device, along with those entering and leaving.
- Respect the local positive definite nature of carrier density since negative density is unphysical.
- Respect the monotonicity of the solution i.e., it should not introduce spurious space oscillations.

Conservative schemes are usually achieved by subdivision of the computational domain into patches (boxes) surrounding the mesh points. The General workflow of the simulation is shown below in Figure 1.3. With an initial guess the given equations are solved after a

convergence is achieved. Furthermore, interband and intraband tunneling is also considered. Based upon different tunneling models and their results a decision is made for the optimization run.

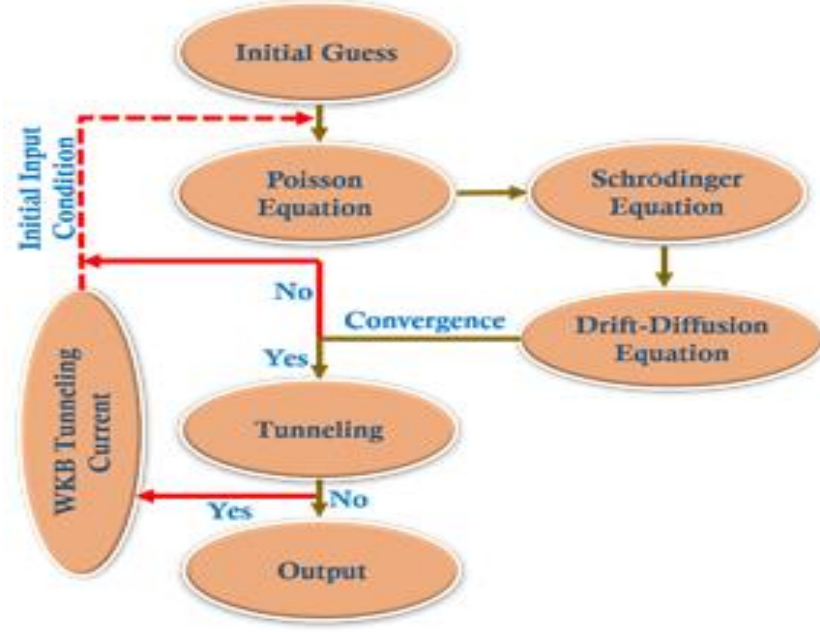


Figure 1.3 General Workflow for a TCAD Simulation.

The General equations governing electrical behavior is described in the APSYS manual as

$$-\nabla \cdot \left(\frac{\epsilon_0 \epsilon_{dc}}{q} \nabla V \right) = -n + p + N_D (1 - f_D) - N_A f_A + \sum_j N_{ij} (\delta_j - f_{ij}) \quad (1.12)$$

$$\nabla \cdot J_n - \sum_j R_n^{ij} - R_{sp} - R_{st} - R_{au} + G_{opt}(t) = \frac{\partial n}{\partial t} + N_D \frac{\partial f_D}{\partial t} \quad (1.13)$$

$$\nabla \cdot J_p + \sum_j R_p^{ij} + R_{sp} + R_{st} + R_{au} - G_{opt}(t) = -\frac{\partial p}{\partial t} + N_A \frac{\partial f_A}{\partial t} \quad (1.14)$$

where equation 1.12 and 1.13 are current continuity equations for carriers while equation 1.11 is Poisson equation.

These equations can be obtained by modifying the scattering factor Q in the RHS of the BTE equation 1.3 by considering electron-electron, electron-ion scattering and other effects. The Poisson and Schrodinger equations as shown in Figure 1.3 are calculated at first to model the structure. Furthermore, the drift-diffusion equation is also calculated numerically. For computational purpose all given equation are discretized. A solution is reached with a chosen convergence criterion since a solution to this non-linear model cannot be obtained definitely using traditional linear methods schemes. Also, a mesh size is needed with a chosen Debye length and a refractive index limit is also required. Steps to construct the LED structure and to simulate in APSYS are:

- Construct the “*.layer” file by setting detailed information for each layer in the growth direction.
- Run the “*.layer” to generate the “*.geo” files and run the “*.geo” to generate the mesh file.
- Run the manual designed “*.sol” file by main equation solver and values for the above mention effects to obtained results for the simulation.

1.4.2 Finite-Difference Time-Domain Method with Lumerical

Finite-Difference Time-Domain (FDTD), the original algorithm proposed by Yee in 1966 [5], is a simple yet powerful state-of-the art method for solving Maxwell’s equations in the time domain for complex 3D geometries and arbitrary materials. It employs second-order central difference approximations of spatial and temporal derivatives of Maxwell’s curl equations. The generalized sequence for the algorithm is:

- Replace derivatives in Maxwell’s equations with finite differences and discretize the time and space.
- Obtain the update equations that determine the future field values from the known, past fields.
- Evaluate the magnetic field one time-step in the future.

- Evaluate the electric field one time-step in the future.
- Repeat previous two steps until the desired time is reached.

The derived finite-difference equations are thus said to be solved in leapfrog style. This scheme is valid for electromagnetic fields in linear, isotropic, lossless media. Modern simulation packages, such as Lumerical FDTD Solutions, build on top of the original algorithm by implementing several sophisticated techniques to model arbitrary materials, thus improving the simulations in terms of accuracy and computation time. The simulation environment already comes with a material database including experimental values of common materials used in photonics. A fit is automatically generated, and for a better agreement several parameters can be tweaked. Monitors, in bright yellow color lines, are the tools that receive information based on the mathematical equations running within the simulation region, and store data which we can later extract. With a variety of monitors are available and should be used for better analysis of the simulation. Apart from the monitor, simulation boundary is also an important part of these simulations. The following figures, Figure 1.4 illustrates the aforementioned parts of the software. A detailed description of the simulation elements and their environment with their functions can be found in the ANSYS Lumerical Website with tutorials [6].

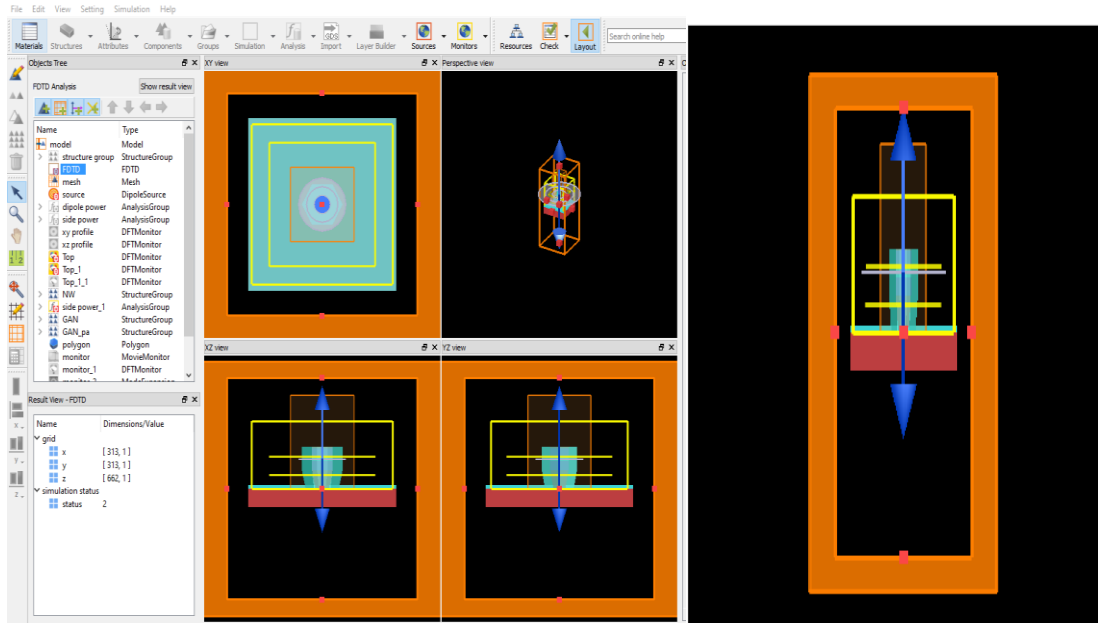


Figure 1.4 Snapshot of Lumerical Layout for the Purpose of Design and Simulation with Different Parts.

1.5 Thesis Preview

In this thesis, focus is on simulation and analysis UV-LEDs, to explore different aspects of LED. So, a study to find optimal IQE of an AlGaIn LED emitting at 255nm was done by varying the quantum well number to determine best structure with optimal power using APSYS, further an improved electron leakage structure is reported which has better droop result for ~284 nm wavelength. Additionally, LEE for AlInN was studied using FDTD method and an improvement of 69% in LEE was achieved for TM polarized light and an improvement is noticed in TE polarized light LEE using passivation technique. The flow of this thesis is given below.

Chapter 1 gives a general overview of LEDs and UV-LED and the description of different simulation tools used in this thesis for analysis.

Chapter 2 introduces the internal quantum efficiency model with brief description of different factors affecting radiative recombination, auger recombination, Shockley-

Read-Hall (SRH) recombination and electron overflow. Additionally, the simulated model is set up using Crosslight APSYS software for finding optimal number of quantum well, and the results show 5 quantum wells is effective at 255nm wavelength but also indicates an ineffective strategy of increasing the quantum well number to reduce the electron leakage.

Chapter 3 gives a method to mitigate the electron leakage problem using concave barrier structure. Primarily, the interaction of electrons in concave structure with LO phonons result in reduced thermal velocity of these interaction electrons leading to a controlled mean free path Thus, resulting in reduced electron leakage and increased power in comparison to conventional LED design.

Chapter 4 gives a perspective on LEE by studying same in AlInN nanowire UV-LED with respect to Polarized light sources and recognizing dominant light mode. An improvement is obtained using HfO₂ with details pertaining to factors involved in changing effectiveness of light w.r.t. to its thickness.

Chapter 5 delves into further studies required to improve these LEDs through a need for doping and exploring Photonic crystal structures.

CHAPTER 2

FACTORS AFFECTING INTERNAL QUANTUM EFFICIENCY AND EFFICIENCY DROOP

2.1 Radiative Recombination

The electronic band structures of solids can be generally described by conduction band, band gap and valence band structures, respectively. The carrier recombination is the reverse of the carrier generation process and these can be classified based on the interaction with photons, phonons, other electrons, or other holes during the processes.

Generally, for light-matter interaction, absorption, spontaneous emission, and stimulated emission are considered. To describe these superficially, consider a direct bandgap semiconductor with a simplified band structure of two discrete energy states. During the absorption, the incident photon with an energy $E = h\nu$ equal or greater than the energy difference $E_c - E_v$ can get absorbed which generates an electron which a transition to the higher energy state after excitation, and hole which stay in lower energy pair. But the electron recombines with the hole after a characteristic spontaneous emission lifetime t_{au} and emits a photon with a random phase, polarization, and direction for spontaneous emission. However, for stimulated emission type of recombination is a result of interaction with another incident photon, with emission of a photon with a coherent phase, polarization, and direction. The Radiative Recombination Rate is given by equation 2.1

$$R_{rad} = Bnp \quad (2.1)$$

Where n and p are free electrons and hole concentration, while B is commonly known as radiative capture probability and is a constant.

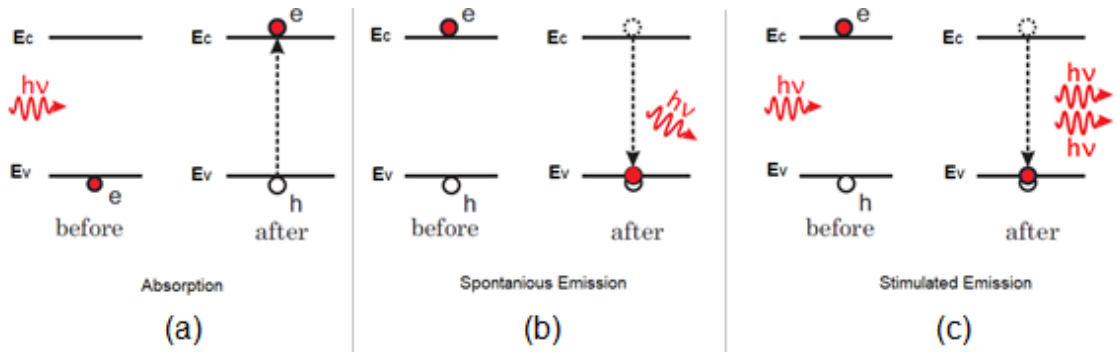


Figure 2.1 Illustration of Simplified Light-Matter Interaction i.e., Absorption Mechanism is shown in (a), Spontaneous Emission Depicted in (b), while (c) shows a Stimulated Emission Mechanism.

2.2 Non-Radiative Recombination

2.2.1 Auger Recombination:

When a potential is applied across the junction, the electrons are energized and some of these high-energy electrons collide with atoms in the semiconductor materials then transfer energy. In Auger processes, carriers scatter across bands and instead of emitting photons, the released energy from electron/hole pairs recombination is transferred to some second electrons. These excited electrons now collide with atoms of the semiconductor materials and relax back in the low-energy orbitals. While in the impact ionization effect, the energy is transferred to the electrons in lower energy orbitals. These excited electrons now jump to the higher energy orbitals and create electron/hole pairs. The impact ionization occurs under high electric fields, and the electrons gain energy larger than the bandgap of the semiconductor, which causes carrier multiplication and the current in the semiconductor to increase dramatically. The probability of the Auger recombination process increases when the carrier density increases since it requires energy exchange between carriers. The Auger recombination R_A rate can be expressed as [8]:

$$R_A = C_n n^2 p + C_p p^2 n$$

simplified as

$$R_A = CN^3 \quad (2.2)$$

Where C_n and C_p are constants called Auger capture probabilities or Auger coefficients for a given semiconductor and n , p are free electron and hole densities while where N is the carrier density in a QW.

2.2.2 Shockley-Read-Hall Recombination:

The crystal defects or impurities modify the band structures and introduce trap levels in the forbidden band between the conduction band and valence band. In SRH recombination process occurs due to the presence of said defects and is a two-step recombination process. The free electrons in the conduction band can relax back and be trapped in the trap levels. After a short period, the electrons in the trap levels relax back to the valence band with the emission of photons or phonons.

For a single trap state SRH expression is obtained as shown below,

Further for localized transitions

$$R_n = BnN_t(1 - f_t)$$

Where N_t is density and f_t is the distribution function for traps. Further for electrons $B=B_n$,

$$B_n = v_n \sigma_n$$

Where v_n is there thermal velocity of electrons and σ_n is the capture cross-section. The lifetime of these captured electrons in a trap is given below as

$$\tau_{n,SRH} = \frac{1}{B_n N_t}$$

These electrons are release at rate T_n and expressed as:

$$T_n = \frac{N_t f_t}{\tau_{rel}}$$

And this τ_{rel} is the release time from a trap and can be determined from equilibrium condition,

$$R_n = T_n$$

Further representing electron density in conduction band as n_t and hole density in valance band as h_t ,

$$T_n = B_n n_t N_t f_t$$

With similar terminology for the holes the expressions are given as

$$R_h = B_h h_t N_t f_t$$

$$B_h = v_h \sigma_h$$

$$\tau_{h,SRH} = \frac{1}{B_h N_t}$$

$$T_h = B_h p_t N_t (1 - f_t)$$

And at equilibrium $R_h - T_h = R_n - T_n$ and on solving further by substituting the expression, we get,

$$f_t = \frac{B_n n + B_h h_t}{B_n (n + n_t) + B_h (h + h_t)}$$

Then upon substitution of f_t in equilibrium equation, we get,

$$R_n - T_n = \frac{B_n N_t B_h (nh - n_i h_i)}{B_n (n + n_i) + B_h (h + h_i)}$$

With $n_i h_i = n_i^2$,

$$R_{SRH} = R_n - T_n = \frac{B_n N_t B_h (nh - n_i^2)}{B_n (n + n_i) + B_h (h + h_i)}$$

$$R_{SRH} = \frac{(nh - n_i^2)}{\frac{B_n (n + n_i)}{B_n N_t B_h} + \frac{B_h (h + h_i)}{B_n N_t B_h}} = \frac{(nh - n_i^2)}{\frac{(n + n_i)}{N_t B_h} + \frac{(h + h_i)}{B_n N_t}} = \frac{(nh - n_i^2)}{\tau_{h,SRH} (n + n_i) + \tau_{n,SRH} (h + h_i)} \quad (2.3)$$

The SRH recombination rate can be calculated using above equation 2.3 [8]. Where n_i is the intrinsic carrier concentration of the given materials, τ_p and τ_n are the recombination lifetime for holes and electrons, respectively. The parameters n_1 and p_1 depend on the trap level E .

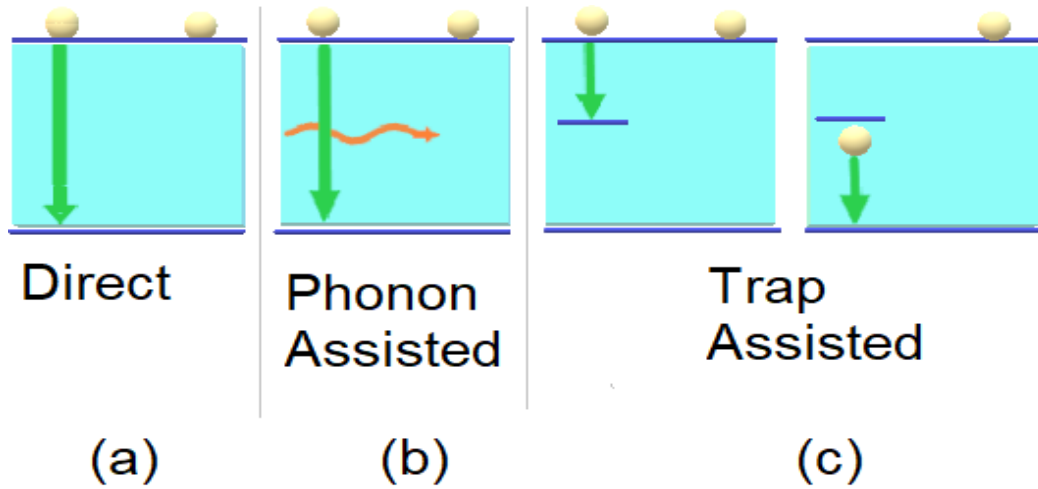


Figure 2.2 Illustration of Different Recombination Processes.

2.2.3 Surface Recombination:

Terminal surface atoms do not have the same bonding structure as bulk atoms due to the lack of neighboring atoms. Resulting in some of the valence orbitals not forming a chemical bond. These dangling bonds are electronic states that can be located in the forbidden gap of the semiconductor, where they act as recombination centers. Surface recombination leads to a reduced luminescence efficiency with heating of the surface due to non-radiative recombination. Surface recombination can occur only when both types of carriers are present. It is important that the carrier-injected in the active region, which have both types of carriers, be far away from any surface. Usually, this is achieved by carrier injection under a contact that is much smaller than a semiconductor die.

It is also difficult to fabricate materials of bulk-planar geometry with impurity levels lower than parts per billion or without defects which tells us that the above processes are unavoidable. To estimate Surface recombination equation 2.4 can be used where A_{nr} is constant for a material with N as carrier density in a QW.

$$R_{surf} = A_{nr} N \quad (2.4)$$

This leads to competition between radiative and non-radiative recombination. The total probability of recombination is given by the sum of the radiative and non-radiative probabilities:

$$\tau^{-1} = \tau_r^{-1} + \tau_{nr}^{-1} \quad (2.5)$$

where τ_r and τ_{nr} are radiative and non-radiative lifetimes.

Theoretically and ideally, in a LED, every single injected electron should generate a photon that is emitted from it. But, practically, the electrical to optical energy conversion accompanies losses during the process.

$$\eta_{EQE} = \eta_{IQE} \times \eta_{EXT} \quad (2.6)$$

η_{EXT} is the optical extraction efficiency and given as the ratio of photons emitted from the LED to the photons generated in the LED quantum well active region. This factor accounts for the photons lost inside the LED. η_{IQE} is the ratio of the photons generated inside the quantum wells (QWs) to the total number of electrons injected, known as internal quantum efficiency. The carrier injection efficiency η_{INJ} is defined for the active region of the device and paired with IQE. Furthermore, we can define η_{IQE} as a fraction of the injected current which can generate photon and is simplifies as:

$$\eta_{IQE} = \frac{I_{rad}}{I_{tot}} \quad (2.7)$$

Where $I_{tot} = I_{rad} + I_{Auger} + I_{SRH} + I_{leak}$ (2.8)

$$\eta_{inj} = \frac{(I_{tot} - I_{leak})}{I_{total}} \quad (2.9)$$

$$\eta_{IQE} = \eta_{inj} \cdot \frac{B.N^2}{(A.N + B.N^2 + C.N^3)} \quad (2.10)$$

Equation 2.8 is known as the ABC model based on equations 2.1, 2.2, and 2.3, where N is the carrier density in QWs and A, B, C are the SRH recombination coefficient, the radiative coefficient, and the Auger coefficient, respectively.

2.3 Electron Overflow

The Piezoelectric polarization is present in GaN-based material, and the absence of centrosymmetry in the wurtzite crystal structure aggravates the carrier overflow problem. In a forward-biased LED, the electrons are accelerated by the built-in electric field and

surpass the quantum well region, leading to efficiency droop. An extra layer is added in-between the *p*-type regions and QW regions to overcome this problem, which is called the electron blocking layer (EBL) [9]. This layer with appropriate Al composition can block the electrons which overflow through the quantum wells, usually improve the performance of AlGaN LED. Additionally, this can also be addressed using a thin material of different composition to the quantum barrier in the barrier region, as shown in chapter 4.

All the above-mentioned effects are used and simulated in APSYS, Advanced Physical Models of Semiconductor Devices, is based on the 2D/3D finite element analysis of the electrical, optical, and thermal properties of modern semiconductor devices.[10]

2.4 Simulation Setup

To investigate the impact of the number of quantum wells on the efficiency of AlGaN based UV-LEDs, simulations for the LED structure described below were carried out with APSYS modeling software.

A LED grown on a *c*-plane AlN template considered for simulation shown in Figure 2.3, contains a 3 μm thick *n*-Al_{0.7}Ga_{0.3}N layer (Si: $5 \times 10^{18} \text{ cm}^{-3}$), followed by an active region comprising varying number for pairs of 3 nm intrinsic Al_{0.6}Ga_{0.4}N QW and 12 nm intrinsic Al_{0.7}Ga_{0.3}N QB layers, succeeded by a 20 nm *p*-Al_{0.85}Ga_{0.15}N EBL (Mg: $3 \times 10^{19} \text{ cm}^{-3}$), then a 100 nm *p*-Al_{0.7}Ga_{0.3}N hole injection layer (Mg: $2 \times 10^{19} \text{ cm}^{-3}$), and finally a 20 nm *p*-GaN contact layer (Mg: $1 \times 10^{20} \text{ cm}^{-3}$). The bandgap of GaN and AlN are considered as 3.42 eV, 6.2 eV, respectively [11]. The bowing parameter and band offset ratio of AlGaN are assumed to be 0.94 eV and 0.67/0.33, respectively [12].



Figure 2.3 Schematic Diagram of the Simulated AlGaN UV LED at 255nm.

By using the 6×6 $k.p$ model [13], the energy band diagrams of all LED structures are calculated. The Shockley–Read–Hall (SRH) recombination lifetime, radiative recombination coefficient, Auger recombination coefficient, and light extraction efficiency are considered as 15 ns, $2.13 \times 10^{-11} \text{ cm}^3/\text{s}$, $2.88 \times 10^{-30} \text{ cm}^6/\text{s}$, and 15%, respectively [14]. Also, the activation energy of Mg-doped $p\text{-Al}_{0.85}\text{Ga}_{0.15}\text{N}$, $p\text{-Al}_{0.7}\text{Ga}_{0.3}\text{N}$, and $p\text{-GaN}$ is considered as 459meV, 408meV, and 170meV, respectively [15,16], while the value for Si-doped $n\text{-Al}_{0.7}\text{Ga}_{0.3}\text{N}$ is set as 15meV [17]. The degree of polarization due to spontaneous and piezoelectric polarization is considered as 50% of the theoretical value and is estimated using the methods proposed by Fiorentini *et al.* [18]. The internal absorption loss is assumed as 2000 m^{-1} , and all simulations are performed at room temperature.

2.5 Results and Discussion

The Radiative recombination rates, Auger recombination rate, SRH recombination rate and hole concentration in the wells are given below in table form to show general trends and plots. The Radiative recombination table clearly shows a decrease in peaks as we increase the no of quantum wells, but the IQE and power plot show the other side of the picture. From IQE and Power vs Current plot, we can clearly see the power increases with an

increase in quantum well, but this trend is not continuous as shown in 7 and 8 quantum well design. Additionally, the droop in IQE is found to be decreasing as we increase the number of quantum well. But an overall decreasing IQE trend is seen, which indicates that an optimal design of 5 quantum well is suitable. And we also know that electron distribution across the wells decreases as we move towards *p*-region from *n*-region as well as when we increase quantum wells. This non-uniform carrier distribution within the quantum wells could be one of the major causes for the decrease in LED IQE when the number of quantum wells is large leading to a decreased electron hole overlap. With, decreased electron and hole transport across the active region when we increase quantum wells results in a lower recombination rate, thus leading to a decreased IQE when increase the quantum from 5 to 7 or 8 wells.

Table 2.1 Results Presenting Peak Radiative Recombination Values for Each Well with Varying Number of Quantum Wells

Quantum well	Peak Value of Radiative Recombination ($E_{28} \text{ cm}^{-3}\text{s}^{-1}$)							
	1 st QW	2 nd QW	3 rd QW	4 th QW	5 th QW	6 th QW	7 th QW	8 th QW
1	13.19	-	-	-	-	-	-	-
2	7.53	8.16	-	-	-	-	-	-
3	4.95	5.37	5.7	-	-	-	-	-
4	4.06	4.40	4.67	5.00	-	-	-	-
5	3.24	3.50	3.68	3.95	4.25	-	-	-
6	2.66	2.86	3.00	3.18	3.45	3.75	-	-
7	2.26	2.43	2.53	2.67	2.87	3.14	3.45	-
8	1.96	2.10	2.17	2.28	2.43	2.64	2.92	3.22

It is clearly seen from Table 2.2 that Auger Recombination is a dominant process that contributes to decreasing IQE rather than SRH recombination. But in contrast, the SRH Recombination is dominant in 1st QW of 8 quantum well design. With higher hole

concentration near p region, we see higher values of Auger recombination as expected. But as the number of quantum wells increases, their peak value decreases.

Table 2.2 Results Presenting Peak Auger Recombination Values for Each Well with Varying Number of Quantum Wells

Quantum well	Peak Value of Auger Recombination ($E28 \text{ cm}^{-3}\text{s}^{-1}$)							
	1 st QW	2 nd QW	3 rd QW	4 th QW	5 th QW	6 th QW	7 th QW	8 th QW
1	19.88	-	-	-	-	-	-	-
2	7.47	9.75	-	-	-	-	-	-
3	3.98	4.91	5.81	-	-	-	-	-
4	2.82	3.40	3.87	4.52	-	-	-	-
5	1.99	2.38	2.63	3.00	3.52	-	-	-
6	1.47	1.75	1.91	2.12	2.45	2.89	-	-
7	1.14	1.35	1.46	1.60	1.81	2.11	2.50	-
8	0.14	1.07	1.15	1.24	1.38	1.58	1.87	2.23

As expected, these non-radiative mechanisms show drop with the increasing quantum well number due to the reduced availability of holes across the active region.

Table 2.3 Results Presenting Peak SRH Recombination Values for Each Well with Varying Number of Quantum Wells

Quantum well	Peak Value of SRH Recombination ($E28 \text{ cm}^{-3}\text{s}^{-1}$)							
	1 st QW	2 nd QW	3 rd QW	4 th QW	5 th QW	6 th QW	7 th QW	8 th QW
1	2.91	-	-	-	-	-	-	-
2	2.04	2.30	-	-	-	-	-	-
3	1.60	1.66	1.89	-	-	-	-	-
4	1.47	1.51	1.58	1.80	-	-	-	-
5	1.32	1.34	1.39	1.45	1.69	-	-	-
6	1.19	1.20	1.24	1.28	1.36	1.56	-	-
7	1.11	1.11	1.14	1.17	1.23	1.30	1.51	-
8	1.04	1.05	1.05	1.08	1.13	1.18	1.26	1.47

The hole concentration plots with the above results clearly show that due to nearly small change in hole concentration and nearly similar peak values of the Radiative, SRH, and Auger recombination, we see a little to no increase in power when we add a quantum

well to the 7 quantum well structure. Furthermore, a general decreasing hole concentration with increasing quantum well is seen as expected.

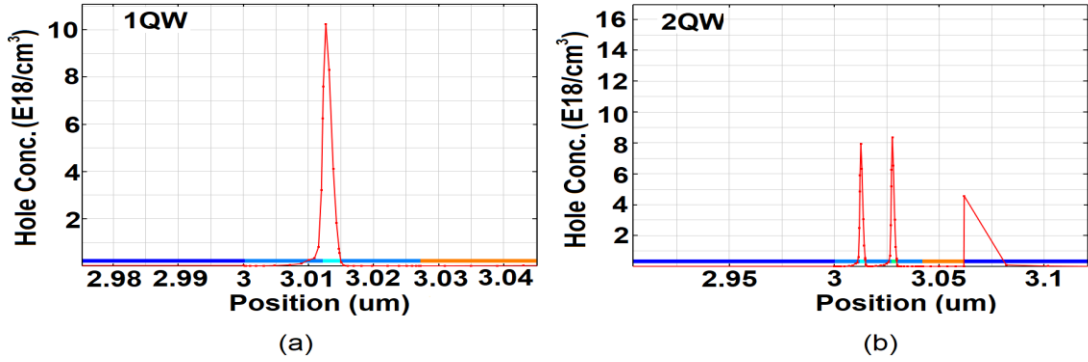


Figure 2.4 Plots for Hole Concentration in a Quantum Well for 1 Quantum Well in (a), and 2 Quantum Well Design in (b).

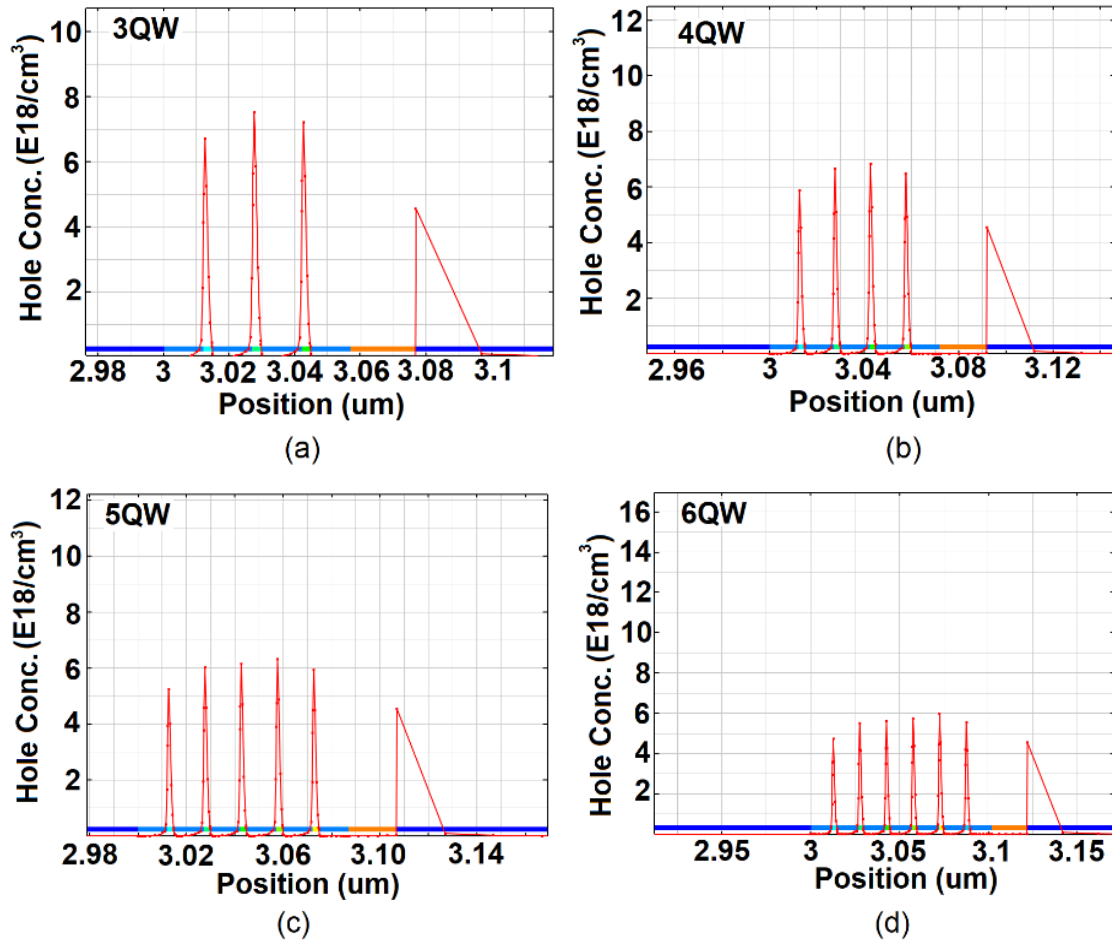


Figure 2.5 Plots for Hole Concentration in a Quantum Well for 3-8 Quantum Well Design show in (a)-(d).

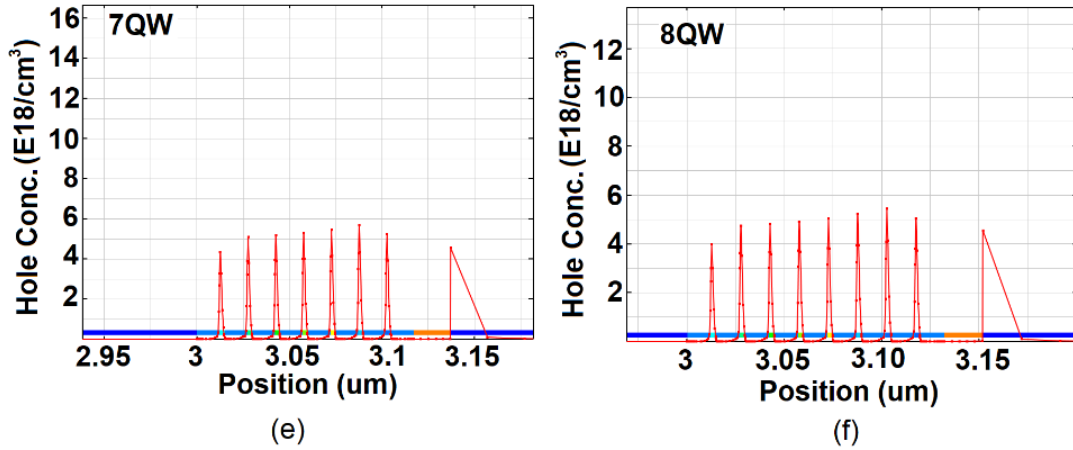


Figure 2.6 Plots for Hole Concentration in a Quantum Well for 7-8 Quantum Well Design show in (e)-(f).

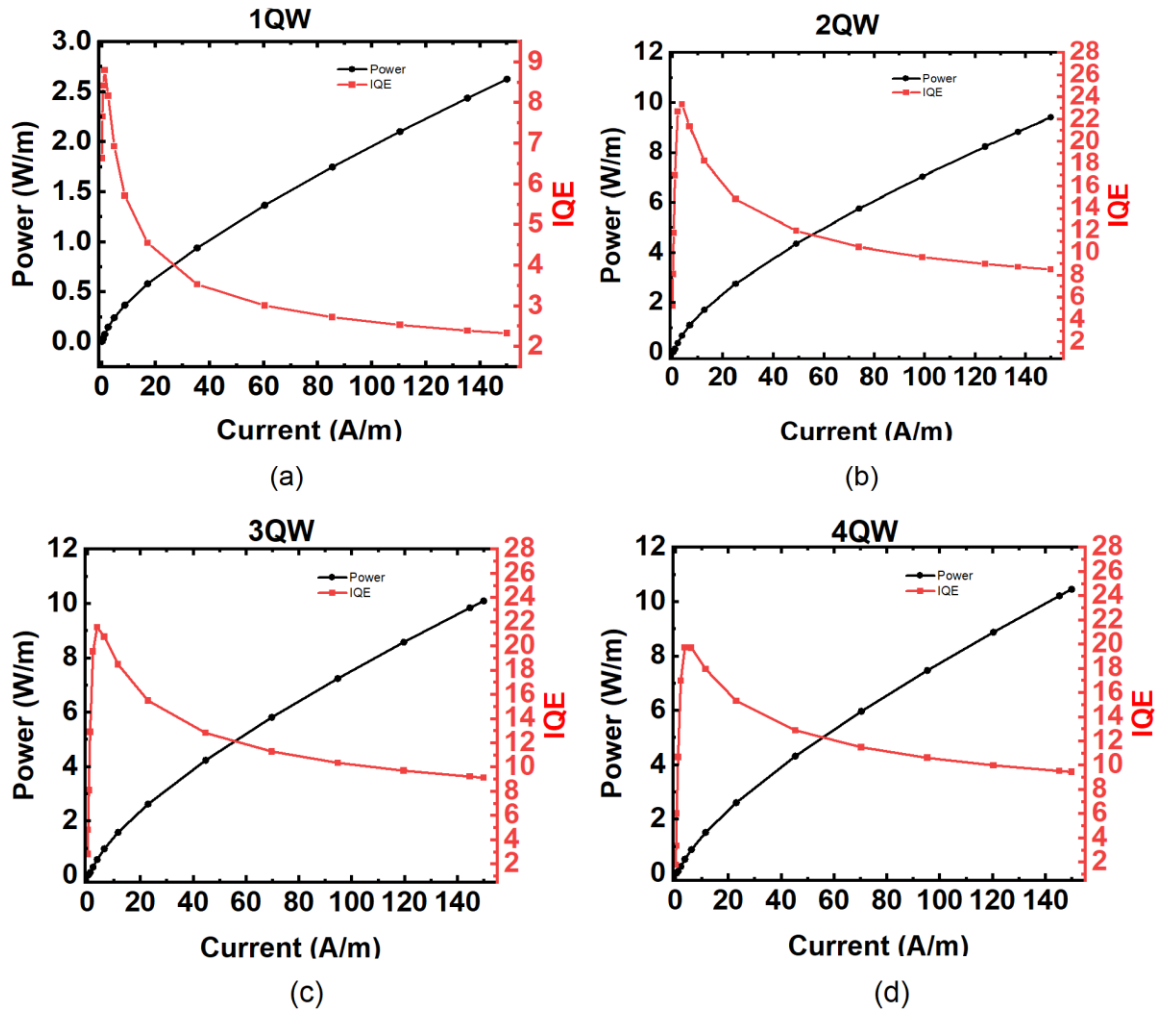


Figure 2.7 Plots for Power vs Current and IQE vs Current for 1- 4 Quantum Well Design shown in (a)-(d).

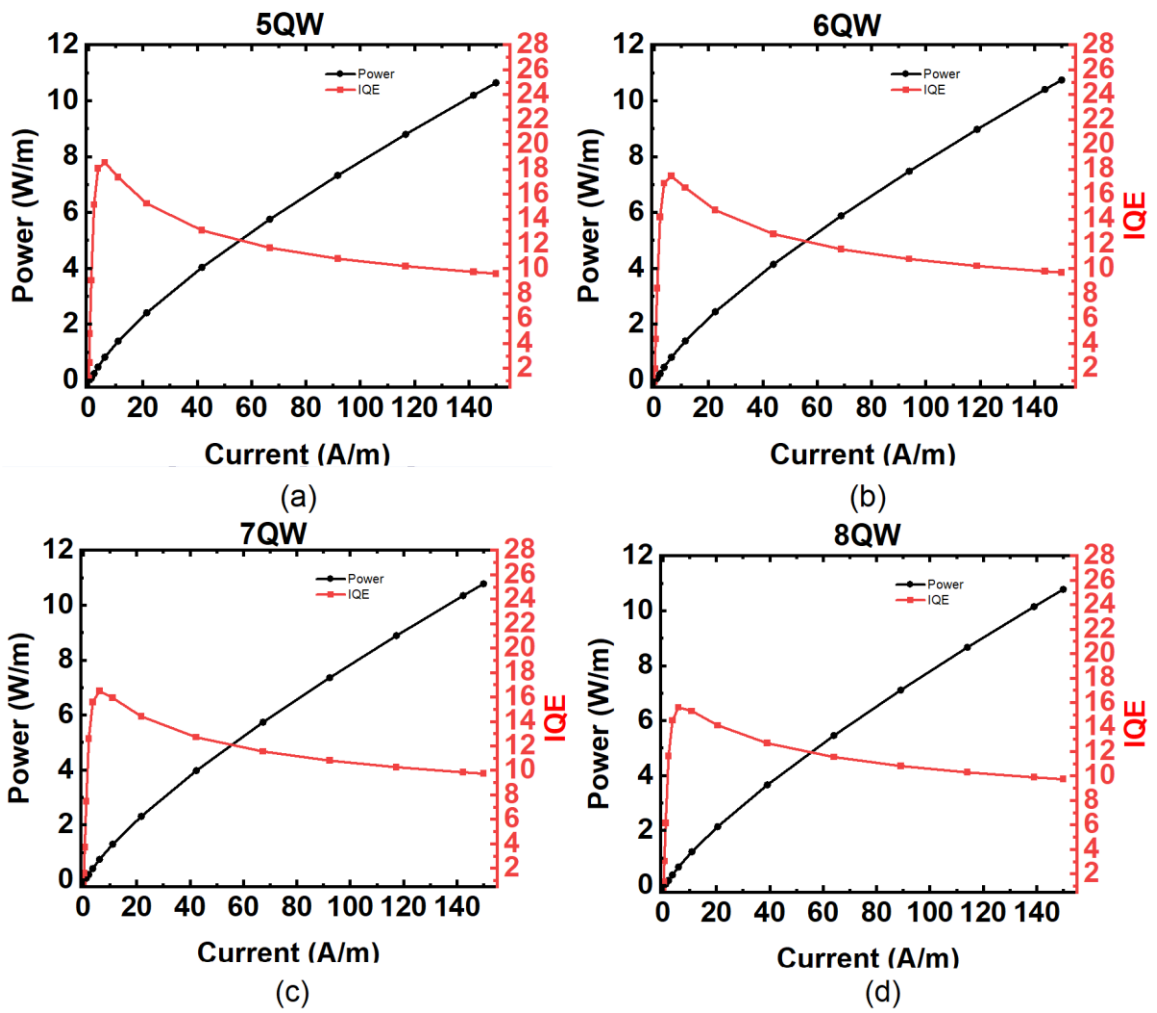


Figure 2.8 Plots for Power vs Current and IQE vs Current for 5-8 Quantum Well Design shown in (a)-(d).

CHAPTER 3

MITIGATING THE ELECTRON LEAKAGE IN ALGAN DEEP UV LEDs USING CONCAVE QUANTUM BARRIER STRUCTURES

3.1 Introduction

Different approaches have been introduced to mitigate the electron overflow to the p -region and improve the carrier confinement in the active region. The EBL is usually re-engineered using, polarization modulated layers [19], a graded layer [20], graded superlattice structure [21, 22], superlattice structure [23], and others to efficiently reduce the electron overflow. Also, integration of the p -doped higher Al composition electron blocking layer (EBL) after the active region is a common approach to stop the electron overflow [24]. Alternatively, the electron overflow has been reduced by increasing the effective conduction band barrier heights (CBBH) with the re-design of quantum barriers (QBs) and promptly utilizing the higher Al composition [25-27]. An alternative approach to alleviate the electron overflow without increasing the Al composition in the QBs and EBL by utilizing the concave QBs instead of conventional QBs in AlGaN UV LEDs is presented in this study.

3.2 Simulation and Structural Parameters

For this study, the conventional AlGaN deep UV LED structure, reported by Yan *et al.* [28] is used as a reference structure, indicated as LED0. Figure 3.1(a) depicts the structure of LED0, which is made up of a $3\mu\text{m}$ $n\text{-Al}_{0.6}\text{Ga}_{0.4}\text{N}$ layer (Si doping: $5\times 10^{18}\text{ cm}^{-3}$), six undoped 12-nm $\text{Al}_{0.5}\text{Ga}_{0.5}\text{N}$ QBs stacked between five undoped 3-nm $\text{Al}_{0.4}\text{Ga}_{0.6}\text{N}$ QWs in the active region, a 20 nm $p\text{-Al}_{0.65}\text{Ga}_{0.35}\text{N}$ (Mg doping: $2\times 10^{19}\text{ cm}^{-3}$) EBL, a 50 nm $p\text{-Al}_{0.5}\text{Ga}_{0.5}\text{N}$ (Mg doping: $2\times 10^{19}\text{ cm}^{-3}$), and a contact layer of 120 nm $p\text{-GaN}$ (Mg doping: $1\times 10^{20}\text{ cm}^{-3}$) cladding layer. Detailed Al composition (%) profile information of the conduction band for LED0 is provided in Figure 3.1(b).

The proposed structure, LED1, is similar to LED0 except for QBs, where LED1 possesses the proposed concave QBs that are composed of 4 nm Al_{0.5}Ga_{0.5}N/4 nm Al_{0.47}Ga_{0.53}N/4 nm Al_{0.5}Ga_{0.5}N layers along the growth direction. This can be seen in Figure 3.1(c). The mesa area of both LEDs is 400 × 400 μm². In this investigation, the energy bandgap of GaN and AlN is calculated using equation 1.2 [29].

$$E_g(T) = E_g(0) - \frac{aT^2}{b+T} \quad (3.1)$$

Where a and b are materials constants, and the corresponding values are 0.909meV/K, 830 K for GaN; 1.799meV/K, 1462 K for AlN [29]. $E_g(0)$ and $E_g(T)$ are the energy bandgap at temperatures 0 and T K, respectively.

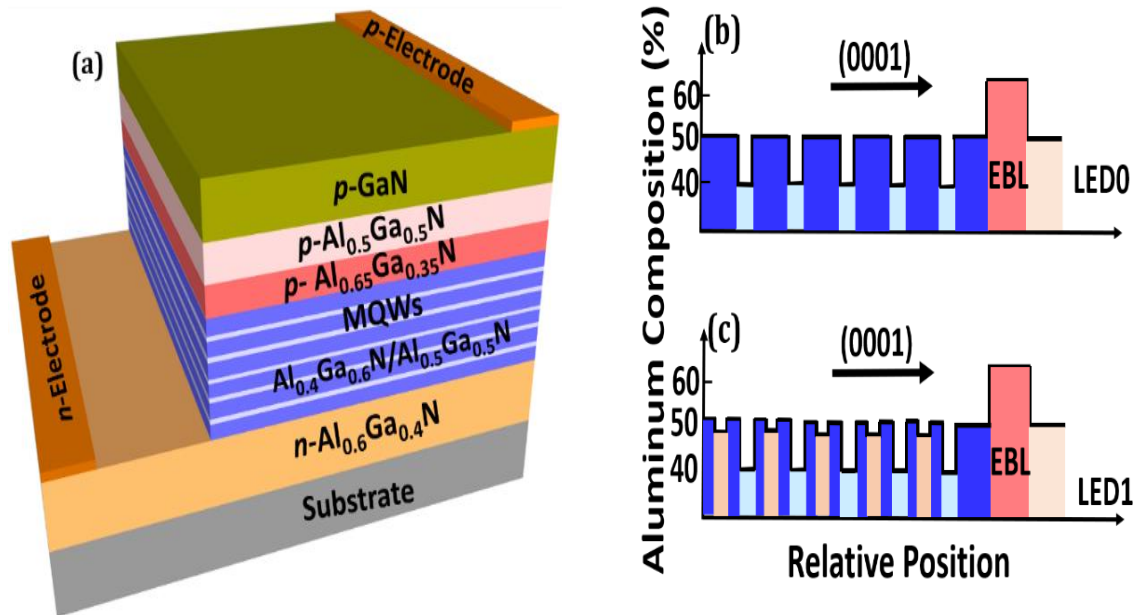


Figure 3.1 (a) Schematic Representation of LED0, Al Composition (%) Profile Related to the Conduction Band of (b) Conventional Structure, i.e., LED0, and (c) Proposed Structure, i.e., LED1.

Source: B. Jain, R. T. Velpula, M. Patel, and H.P.T. Nguyen, Controlled carrier mean free path for the enhanced efficiency of III-nitride deep-ultraviolet light-emitting diodes." *Applied Optics* 60, 11, 3088-3093, (2021).

The energy bandgap of $\text{Al}_x\text{Ga}_{1-x}\text{N}$ is determined using equation 3.2, as given below.

$$E = x \cdot E_{\text{AlN}} + (1-x) \cdot E_{\text{GaN}} - b \cdot x \cdot (1-x) \quad (3.2)$$

While, the values of $E_g(0)$ considered for GaN and AlN are 3.507 eV and 6.23 eV, respectively [29]. With b as the bowing parameter and its value is assumed to be 0.94 [12]. The activation energy for Mg was considered in this model and considered as 170meV and 510meV for p -GaN and p -AlN, respectively, and an estimate for p - $\text{Al}_x\text{Ga}_{(1-x)}\text{N}$ alloy using linear approximation where $0 < x < 1$ [15]. The Auger recombination coefficient, Radiative recombination coefficient, Shockley-Read-Hall (SRH) recombination coefficient, and light extraction efficiency values as $2.88 \times 10^{-30} \text{ cm}^6/\text{s}$, $2.13 \times 10^{-11} \text{ cm}^3/\text{s}$, $6.67 \times 10^7/\text{s}$, and 15%, respectively [14]. Using the methods developed by Fiorentini *et al.* [18], the net polarization effect due to piezoelectric and spontaneous polarization is estimated and set at 50% of the theoretical values in this model. The band offset ratio for the III-nitride material hetero-junctions is taken as 0.67/0.33 [21]. The 6×6 $k.p$ model was used to calculate the energy-band diagrams of two LED structures [13], and other band parameters utilized in the model can be found described in [31]. Moreover, a strict calibration of the simulation parameters and model was made by closely matching simulation results of LED0 with experimental data [32].

3.3 Results

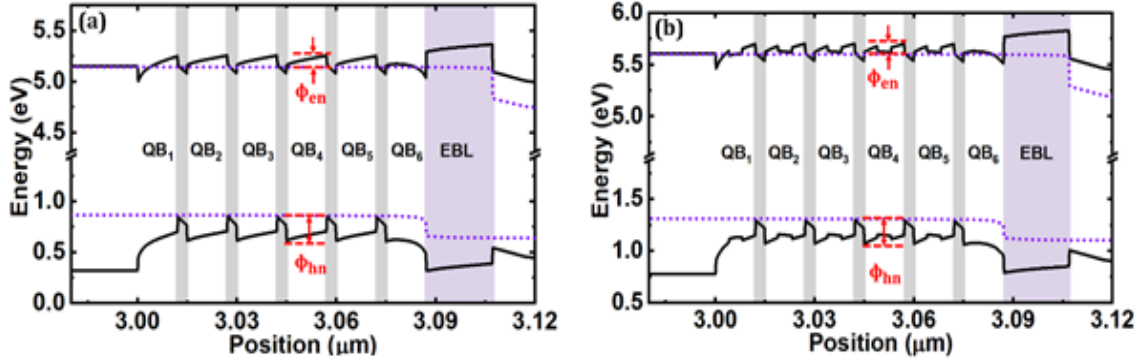


Figure 3.2 Energy Band Diagram of (a) LED0 and (b) LED1 at 60 mA Current Injection.

Source: B. Jain, R. T. Velpula, M. Patel, and H.P.T. Nguyen, Controlled carrier mean free path for the enhanced efficiency of III-nitride deep-ultraviolet light-emitting diodes." *Applied Optics* 60, **11**, 3088-3093, (2021).

The Energy band diagram of both LEDs which is estimated to be at 60 mA current injection is shown in Figure 3.2. Additionally, the values (ϕ_{en}) of, the effective conduction band barrier heights (CBBH) i.e., the maximum energy difference between the conduction band and its corresponding quasi-Fermi level for electrons in the corresponding barrier (n) were estimated from Figure 3.2 and presented in Table 3.1. We can clearly see the proposed structure, LED1, exhibits relatively lower ϕ_{en} values compared to the conventional structure, LED0. It has been reported that the higher ϕ_{en} values support the electron blocking capability in the active region and prevent severe electron leakage into the *p*-region [9]. Irrespective of ϕ_{en} values, LED1 with concave QBs demonstrate less electron leakage due to reduced electron Mean free path in the active region. Further details of the electron Mean free path is explained in this section. Additionally, the effective valence band barrier height (VBBH) values are denoted as ϕ_{hn} , which is the maximum energy difference between the quasi-Fermi level for holes and the valence band at the corresponding barrier (n). These values are estimated from valence bands and provided in Table 3.2. The ϕ_{hn} values are low in LED1 compared to LED0 because of the concave QBs, henceforth promoting better hole transportation into

AlGaN/AlGaIn multi QW region.

Table 3.1. Effective Conduction Band Barrier Heights of QBs (ϕ_{en}) and EBL (ϕ_{EBL}) for LED0 and LED1

CBBH	LED0	LED1
ϕ_{e1}	107.5meV	96.1meV
ϕ_{e2}	114.3meV	98.8meV
ϕ_{e3}	113.8meV	98.1meV
ϕ_{e4}	112.6meV	96.8meV
ϕ_{e5}	110.1meV	94.6meV
ϕ_{e6}	31.2meV	28.5meV

Source: B. Jain, R. T. Velpula, M. Patel, and H.P.T. Nguyen, Controlled carrier mean free path for the enhanced efficiency of III-nitride deep-ultraviolet light-emitting diodes." *Applied Optics* 60, **11**, 3088-3093, (2021).

A theoretical model was introduced with the help of different electron transport schemes for better insight into the controlled electron mean free path of LED1. The schematic energy band diagrams of LED0 and LED1 are shown in Figure 3.3. The number of electrons injected into QB is assumed as N_0 in both LEDs. As shown in Figure3.3(a), electrons carry four different transport processes in the active region of LED0. In this model for simplicity, electron tunneling through barriers is not employed. Process ① denotes a part of the electrons (N_{co}) from N_0 are scattered and captured into the QW. Process ② is used to represent some of the captured electrons that recombined radiatively with holes and non-radiatively with crystal defects.

Table 3.2 Effective Valence Band Barrier Heights of QBs (ϕ_{hn}) for LED0 and LED1

VBBH	LED0	LED1
ϕ_{h2}	251.9meV	237.4meV
ϕ_{h3}	250.3meV	236.7meV
ϕ_{h4}	249.3meV	235.6meV
ϕ_{h5}	248.1meV	234.7meV

Source: B. Jain, R. T. Velpula, M. Patel, and H.P.T. Nguyen, Controlled carrier mean free path for the enhanced efficiency of III-nitride deep-ultraviolet light-emitting diodes." *Applied Optics* 60, **11**, 3088-3093, (2021).

However, some of them can escape from the QW, represented in process (3). In process (4), the electrons with longer electron mean free path can directly jump over QW without being captured in it. It is clearly recognized that processes (3) and (4) lead to electron leakage from the active region, which is undesired and needs to be mitigated. equation 3.3 is the mathematical representation of captured electrons (N_{c0}) in QW of LED0 [26],

$$N_{c0} = N_0 \times [1 - \exp(-\frac{t_{QW}}{l_{MFPO}})] \quad (3.3)$$

where t_{QW} is the QW thickness, and l_{MFPO} is the electron mean free path in LED0. The electron transport processes differ in the proposed structure, LED1, from LED0 by processes (5) and (6) due to the concave QBs.

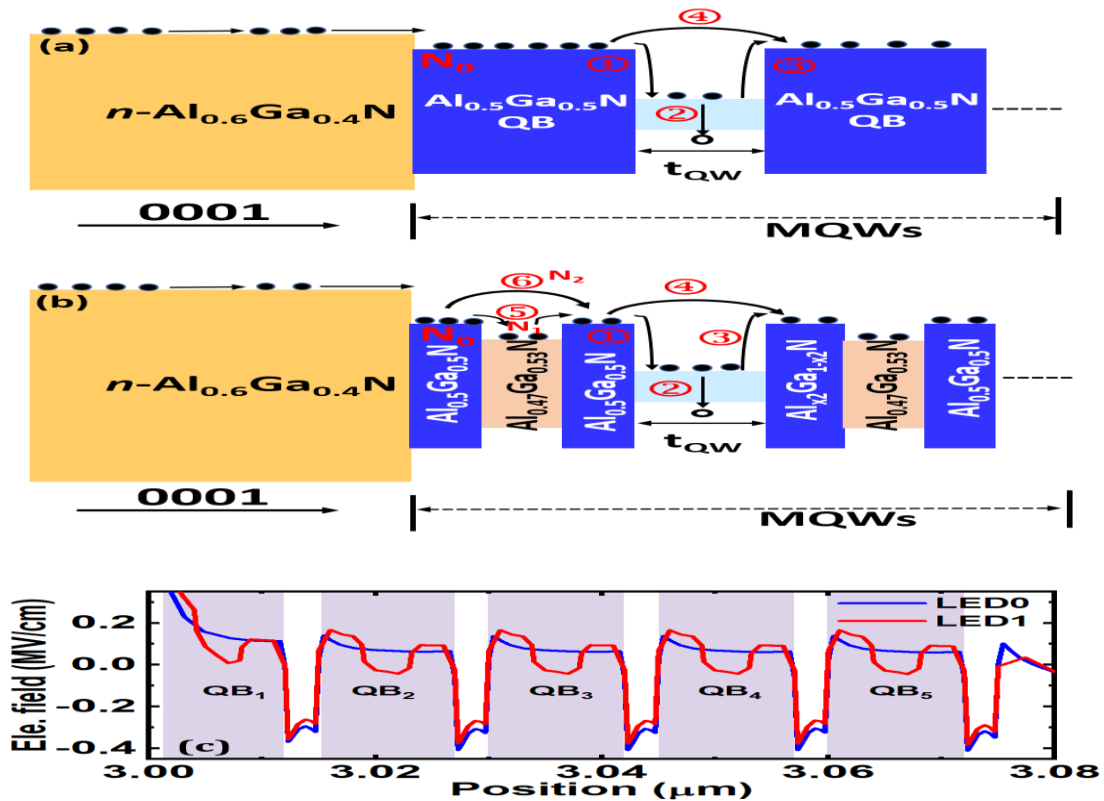


Figure 3.3 Schematic of Energy Band Diagram of (a) LED0 and (b) LED1, (c) Electrostatic Field in MQWs of LED0 and LED1.

Source: B. Jain, R. T. Velpula, M. Patel, and H.P.T. Nguyen, Controlled carrier mean free path for the enhanced efficiency of III-nitride deep-ultraviolet light-emitting diodes." *Applied Optics* 60, 11, 3088-3093, (2021).

In LED1, a part of electrons (N_1) from N_0 are trapped by the $\text{Al}_{0.47}\text{Ga}_{0.53}\text{N}$ layer by interaction of longitudinal optical (LO) phonons before being captured in QWs. These interactions of phonons with electrons usually creates perturbation in the motion of electrons by scattering them from one state to another state, which results in a reduction of carrier mobility and an increase in resistivity, and ultimately cools down the hot electrons [33]. Hence, the electrons have reduced thermal velocity. The reduction in the thermal velocity, v_{th1} due to electron-phonon interaction during process ⑤ is calculated using equation 3.7. Concurrently, the remainder of electrons ($N_2=N_0-N_1$) can pass over the $\text{Al}_{0.47}\text{Ga}_{0.53}\text{N}$ layer. Overall, captured electrons (N_{c1}) in QW of LED1 can be estimated by equation 3.4,

$$N_{c1} = N_1 \times [1 - \exp(-\frac{t_{QW}}{l_{MFP1}})] + N_2 \times [1 - \exp(-\frac{t_{QW}}{l_{MFP2}})] \quad (3.4)$$

The electrons that are undergoing the process ⑤ have the mean free path of l_{MFP1} , and the electrons that participated in process ⑥ have the mean free path of l_{MFP2} . From equations (3.3) and (3.4), one of the possible ways to improve the captured electron concentration in QWs is to reduce the electron mean free path. By focusing on the calculation of electron mean free path in both of the LEDs. The electron mean free path (l_{MFP}) can be expressed as a function of thermal velocity (v_{th}) and the scattering time (τ_{sc})

$$l_{MFP} = v_{th} \times \tau_{sc} \quad (3.5)$$

$$v_{th0} = \sqrt{2 \times \frac{(E_0 + W_0)}{m_e}} \quad (3.6)$$

$$v_{th1} = \sqrt{2 \times \frac{(E_1 + \Delta E + W_1 - \hbar\omega - \Delta E)}{m_e}} = \sqrt{2 \times \frac{(E_1 + W_1 - \hbar\omega)}{m_e}} \quad (3.7)$$

$$v_{th2} = \sqrt{2 \times \frac{(E_1 + W_1)}{m_e}} \quad (3.8)$$

where $E_0 = 83.11\text{meV}$ and $E_1 = 83.92\text{meV}$ are additional kinetic energies in the previous layer of QB_2 with respect to its conduction band of LED0 and LED1. The $W_0 = 88.78\text{meV}$ and $W_1 = 70.55\text{meV}$ are work done to the electrons by the generated local electric field in QB_2 of LED0 and LED1, respectively. The work done values are estimated using electric field $E(y)$, along the growth direction “y” of QB_2 from Figure 3.3 © and can be written as

$$W = \int_0^{t_{QB}} q \times E(y) dy \quad (3.9)$$

Where t_{QB} is the QB thickness. The electron thermal velocity in LED0 is represented by v_{th0} , while v_{th1} and v_{th2} are thermal velocities for electrons undergoing processes ⑤ and ⑥ in LED1. $-\Delta E$ is the energy lost by electrons while jumping from the $n\text{-Al}_{0.47}\text{Ga}_{0.53}\text{N}$ layer during process ⑤ in LED1. At the same time, the $+\Delta E$ in equation (3.7) represents the kinetic energy received by the electrons when crossing the band-offset between $n\text{-Al}_{0.5}\text{Ga}_{0.5}\text{N}$ and $n\text{-Al}_{0.47}\text{Ga}_{0.53}\text{N}$ layers. The effective mass of the electrons is considered as m_e . Also, $\hbar\omega \approx 102\text{meV}$ [34] is the energy lost due to LO phonon emission during the scattering in process ⑤ of LED1. Therefore, by calculating the thermal velocity, values of v_{th0} , v_{th1} , and v_{th2} as 4.82×10^7 cm/s, 2.66×10^7 cm/s, and 4.57×10^7 cm/s respectively are obtained. The electrons who undergo process ⑤ due to the proposed concave QB exhibit the lowest thermal velocity i.e., $v_{th1} < v_{th2} < v_{th0}$ is observed. Subsequently, the electron mean free path at $\tau_{sc} = 0.0045$ ps [35] for above all cases would be 2.169 nm, 1.197 nm, and 2.056 nm, respectively. As expected, electrons that are undergoing process ⑤ demonstrate the lowest mean free path or rephrasing, the process ⑤ is helping to cool down hot electrons in the QBs before being captured in QWs which is similar to an earlier report of InGaN white LEDs where an

integrated coupled QWs is used to slow down the hot electrons [36]. Additionally, the concaved QBs reinforces the overlap of electron-hole wavefunctions spatially that supports the radiative recombination mechanism [37], also exhibits a reduced electrostatic field in MQWs of LED1, as shown in Figure 3.3(c). Overall, the proposed structure has a lower electron mean free path that definitely enhances the electron capture capacity in the QWs and eminently mitigates the electron leakage from the active region. Electron concentration in the active region of LED0 and LED1 is shown in Figure 3.4 (a). As anticipated, due to the reduced electron mean free path, electron concentration in the active region of LED1 is improved. As a result, the electron overflow from the active region of LED1 is reduced compared to LED0. Figure 3.4(b) shows the resulting lower electron leakage was found in the *p*-region of LED1. Such reduced electron leakage also avoids the unwanted non-radiative recombination of leaked electrons with incoming holes in the *p*-region, aiding in efficient hole injection into the multi QWs. Resulting, reduced effective VBBH's in LED1 supports better hole transportation among the QWs. Altogether, Figure 3.4(c) shows the hole concentration in the active region of LED1 which is observed as increased. The integrated hole density in the active region for LED0 and LED1 is calculated to be $7.2 \times 10^{12} \text{ cm}^{-2}$ and $9.25 \times 10^{12} \text{ cm}^{-2}$, respectively. Subsequently, radiative recombination is also significantly improved due to the higher carrier concentration in the multi QWs of LED1 compared to LED0 as shown in Figure 3.4(d). The results from calculated IQE for both the LEDs, are shown in Figure 3.5(a). LED1 exhibits enhanced electrical injection efficiency with reduced electron overflow and increased carrier distribution throughout the device active region due to an effective concave quantum barrier structure. This significantly improved the radiative recombination and reducing the electron overflow in LED1, due to which a maximum IQE of ~39%, by contrast it is ~35% in the case of LED0 which is exhibited. Furthermore, at 60 mA current injection, the IQE of LED1 show an

improvement of ~40.2% compared to LED0. Also, the efficiency droop is reduced by ~23.3% in LED1 during 0-60 mA operation.

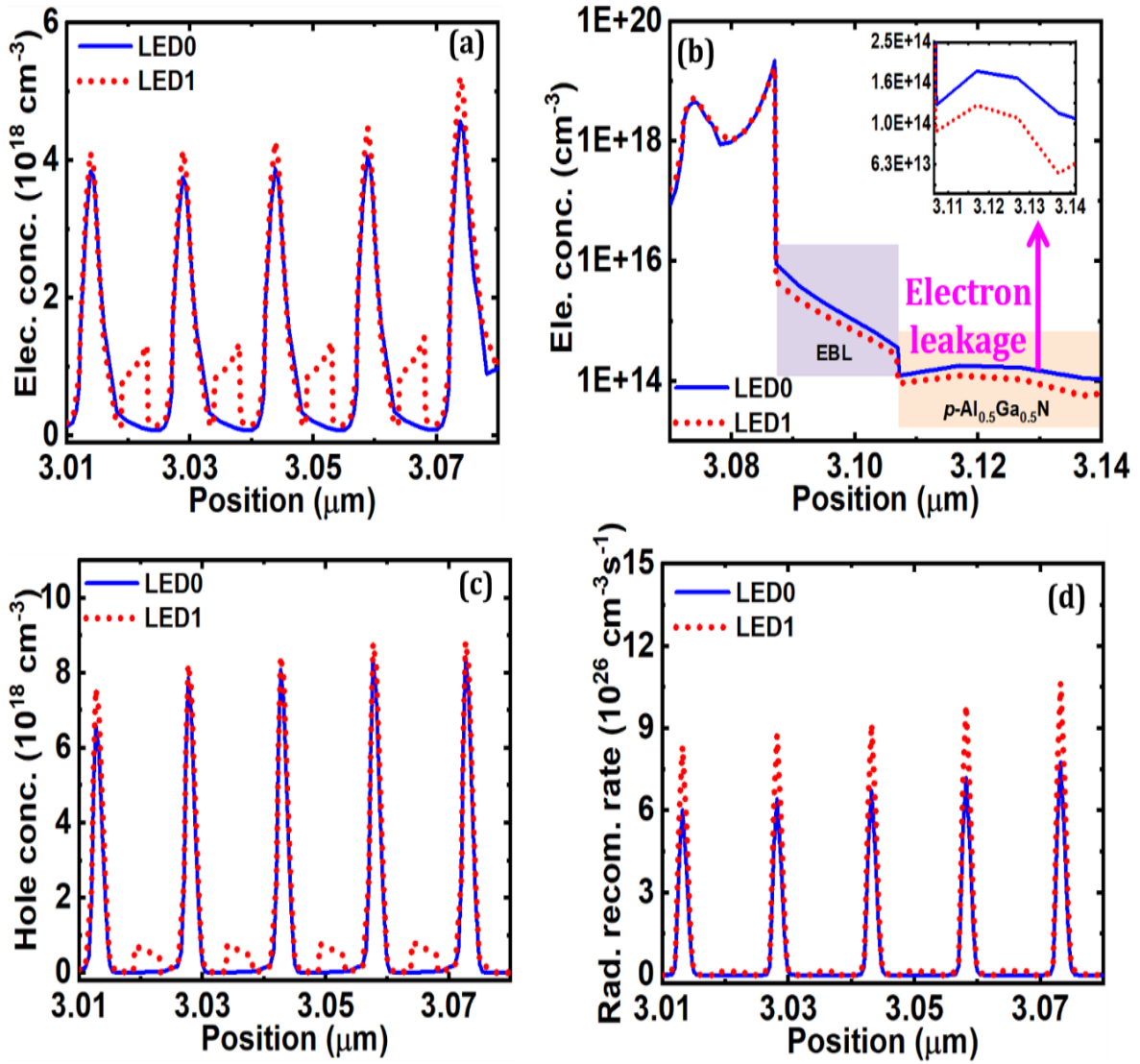


Figure 3.4 (a) Electron Concentration, (b) Electron Leakage, (c) Hole Concentration, and (d) Radiative Recombination Rate in MQWs of LED0 and LED1.

Source: B. Jain, R. T. Velpula, M. Patel, and H.P.T. Nguyen, Controlled carrier mean free path for the enhanced efficiency of III-nitride deep-ultraviolet light-emitting diodes." *Applied Optics* 60, **11**, 3088-3093, (2021).

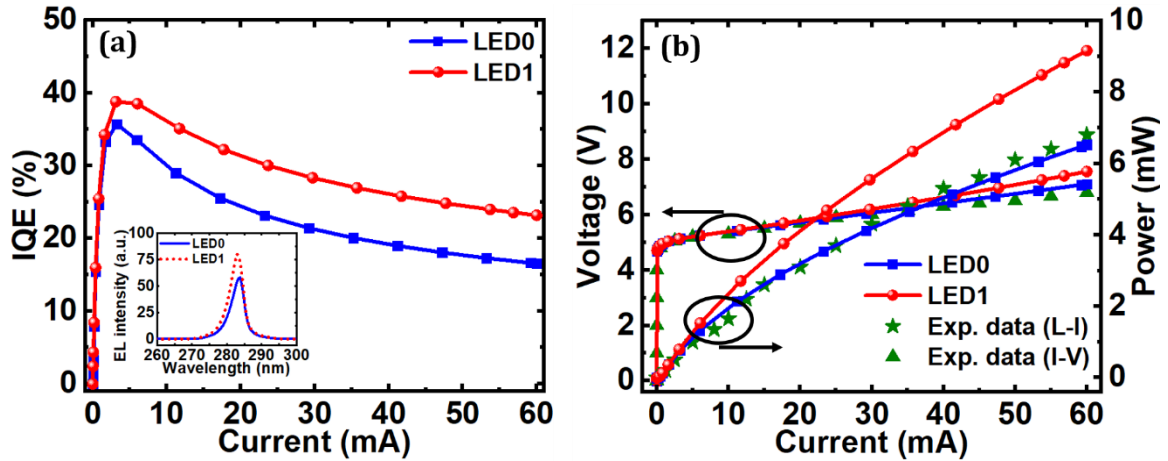


Figure 3.5 Calculated (a) IQE (inset figure: EL intensity), and (b) Power and Voltage Characteristics of LED0 and LED1 as a Function of Injection Current.

Source :B. Jain, R. T. Velpula, M. Patel, and H.P.T. Nguyen, Controlled carrier mean free path for the enhanced efficiency of III-nitride deep-ultraviolet light-emitting diodes." *Applied Optics* 60, **11**, 3088-3093, (2021).

Figure 3.5(a) illustrates the expected electroluminescence (EL) spectra for both of the LEDs. Again, due to improved radiative recombination, the EL intensity of LED1 is higher than LED0 at the emission wavelength of ~ 284 nm. Figure 3.5(b) demonstrates the power vs. current (L-I) characteristics and voltage vs. current (I-V) characteristics for LED0 and LED1. The green stars and triangles are L-I and I-V characteristics for the reference structure that were experimentally reported by Yan *et al.* [12]. As depicted in Figure 3.5 (b), the simulated L-I-V characteristics of LED0 are closely matching with the experimentally reported results, which validates the reliability of the considered simulation model and parameters. The turn-on voltage for LED1 is nearly similar to that of LED0, but with a slightly higher operating bias voltage at 60 mA injection current. A tremendous improvement in the output power of LED1 is to be noted. The recorded output power of LED1 is 9.16mW at 60 mA current injection boosting power by $\sim 40.5\%$ in comparison to LED0 at the same current injection level.

To understand the importance of the concave structure, a further study of different

LED structures was done by increasing the Al composition in the steps of 1% for the QBs of LED0 from $\text{Al}_{0.5}\text{Ga}_{0.5}\text{N}$ to $\text{Al}_{0.55}\text{Ga}_{0.45}\text{N}$. The Al composition in the LED structures with of 51%, 52%, 53%, 54%, and 55% in QBs are named as LEDA, LEDB, LEDC, LEDD, and LEDE, respectively. Figure 3.6 (a). shows the IQE for the LEDs at 60 mA current injection and the IQE droop during 0-60 mA current injection of all structures.

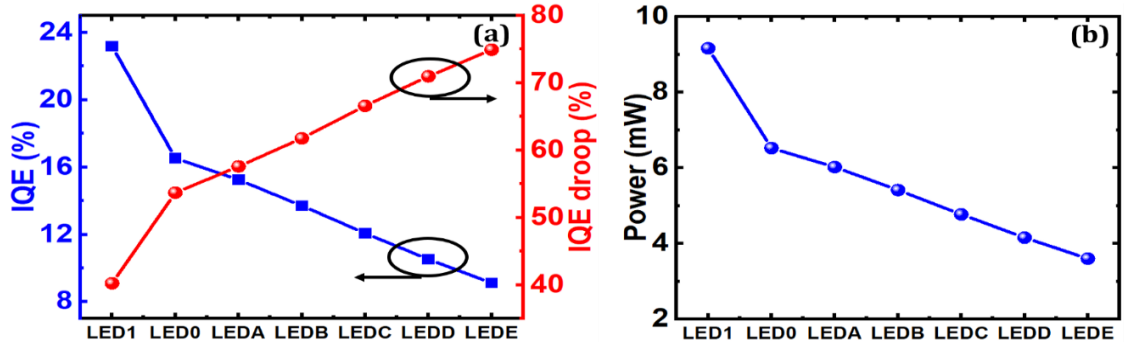


Figure 3.6 (a) IQE at 60 mA and IQE Droop During 0-60 mA Current Injection, (b) Output Power at 60 mA of LED 0, LED 1, LED A, LED B, LED C, LED D, and LED E.

Source: B. Jain, R. T. Velpula, M. Patel, and H.P.T. Nguyen, Controlled carrier mean free path for the enhanced efficiency of III-nitride deep-ultraviolet light-emitting diodes." *Applied Optics* 60, 11, 3088-3093, (2021).

Figure 3.6(b) depicts the comparative output power at 60 mA for the same structures. Figure 3.6 clearly shows that the proposed structure i.e., LED1 exhibits the highest IQE and output power at 60 mA current injection with the lowest IQE droop during 0-60 mA current injection. On the other hand, the LED performance in terms of IQE and output power is deteriorating with the increase of Al composition from 50% (LED0) to 55% (LEDE) in QBs. This is mainly due to increased spontaneous polarization discontinuity at the quantum barrier – quantum well interface, which supports the quantum-confined Stark effect and eventually reduces the radiative recombination in these structures [38]. The proposed concave structure can be realized by experiment due to straightforward design using both molecular beam epitaxy (MBE) and metal-organic chemical vapor deposition (MOCVD).

CHAPTER 4

IMPROVING THE LIGHT EXTRACTION EFFICIENCY OF ALINN NANOWIRE ULTRAVIOLET LIGHT-EMITTING DIODES BY HFO₂ SURFACE PASSIVATION

4.1 Introduction

Nanowire (NW) structure exhibits significantly reduced defect density and piezoelectric polarization as compared to the planar counterpart due to effective strain relaxation through the sidewalls, resulting in reduced quantum-confined Stark effect [39]. However, due to the high surface area to volume ratio in NWs, surface density states such as dangling bonds and fermi level pinning on the NW surface are high, leading to increased non-radiative recombination near the surface [39, 40]. Due to their direct and wide bandgap energy, light emission capability for the entire UV region, III-Nitride semiconductor alloys, especially AlGaN and AlInN, have drawn significant attention [41]. Several efforts have been made on AlGaN planar and NW LEDs to improve their performance, but the performance is still limited in the deep UV region. The poor quality of epitaxial growth includes high threading dislocation density, electron leakage, low light extraction efficiency (LEE), and others are some of the probable reasons for the poor performance [42,43]. Though AlInN can be optically tuned to emit the light from the deep UV to mid-infrared (IR) region, it is relatively unexplored compared to other III-nitride alloys. In this context, study for the LEE properties of a single AlInN NW UV LED at 220 nm – 400 nm wavelength regime using the finite-difference time-domain (FDTD) simulations and further passivation study was done to improve the LEE of AlInN LED by passivation technique.

4.2 Simulation Setup

Three-dimensional (3D) FDTD computational method was used in this study, for estimating the LEE of the AlInN NW UV LEDs [44]. The AlInN NW UV LED structure with 200 nm *n*-GaN, 100 nm *n*-Al_xIn_{1-x}N quantum barrier (QB), 40 nm *i*-Al_yIn_{1-y}N quantum well (QW), 100 nm *p*-Al_xIn_{1-x}N QB, and 20 nm *p*-GaN layer is grown on Si substrate. On this Si substrate, the *n*-GaN layer is tapered with a diameter increasing from 70 nm (bottom) to 100 nm (top). The diameter is set to be 100 nm for the rest of the regions. For the emission of ~282 nm wavelength, the composition of QW is Al_{0.78}In_{0.22}N and Al_{0.825}In_{0.175}N is the composition for QB layers. To avoid the reflection of outgoing waves back to the simulation space, the entire NW structure with 12 perfectly matched layer (PML) boundary conditions was encapsulated [45]. For the emission of ~282 nm wavelength light, the refractive index of Al_{0.825}In_{0.175}N, Al_{0.78}In_{0.22}N, and GaN is considered 2.4132, 2.4365, and 2.623, respectively [46,47]. The attenuation factor (σ) and auxiliary attenuation coefficient(κ) are set as 0.25 and 2 for this PML. Additionally, the absorption coefficient for the same layers taken as 70000 cm⁻¹, 79000 cm⁻¹, and 170000 cm⁻¹ in this model. The refractive index of HfO₂ is considered to be 1.986 [48]. In this study, TM-polarized LEE is estimated by placing a single TM polarized dipole source in the middle of the QW, and TM polarization is represented by the major electric field travels in the out-of-plane direction [E // c-axis]. Similarly, a single TE polarized dipole source was placed in the middle of the QW to estimate the TE polarized LEE, and TE polarization is considered as the major electric field that travels in the in-plane direction [E// c-axis]. Further, to measure the total power generated in the active region accurately, source power monitors are placed around the single dipole source. Output power monitors, placed around

the NW LED is used to measure the total output power radiated by our NW LED, are kept at a total distance of twice the NW diameter and an emission wavelength. Finally, the ratio of the light output power measured by the output power monitors to the total emitted power in the active region measured by the source power monitor was used to define the Light extraction efficiency of this NW LED. This method is commonly employed in studying the optical properties of NW structure LEDs in theoretical works [49-51]). Also, a planar structure was simulated to estimate its LEE. The material parameters were kept same just the LED geometry was increased to 1000 nm*1000 nm to a rectangular shape, with appropriate power monitor distance.

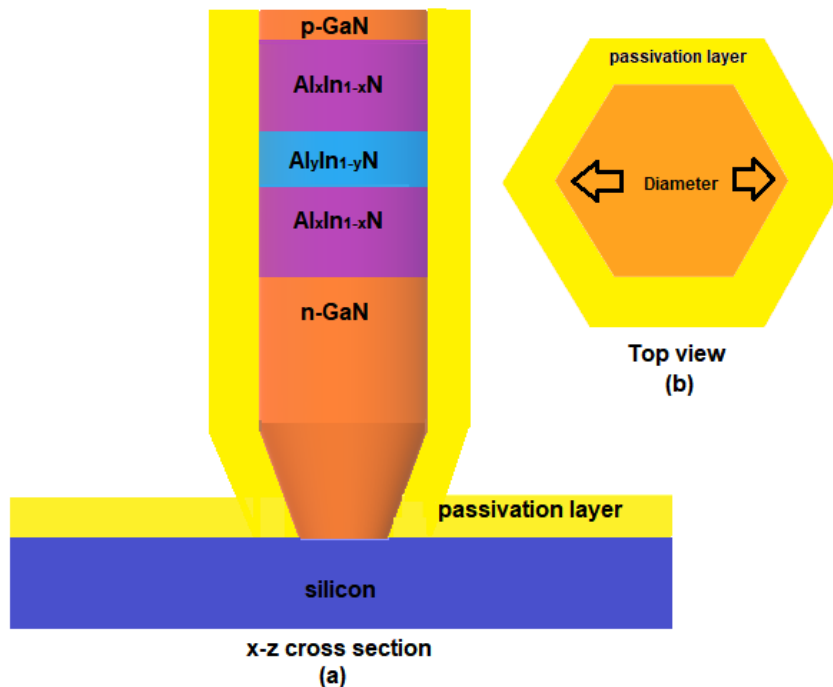


Figure 4.1 (a) Schematic Illustration of AlInN-based NW UV LED with HfO₂ Passivation Layer, (b) Cross-Sectional View of NW from the Top.

Source: M. Patel, B. Jain, R. T. Velpula, and H. P. T. Nguyen, "Effect of HfO₂ Passivation Layer on Light Extraction Efficiency of AlInN Nanowire Ultraviolet Light-Emitting Diodes." *ECS Transaction*, In Press.

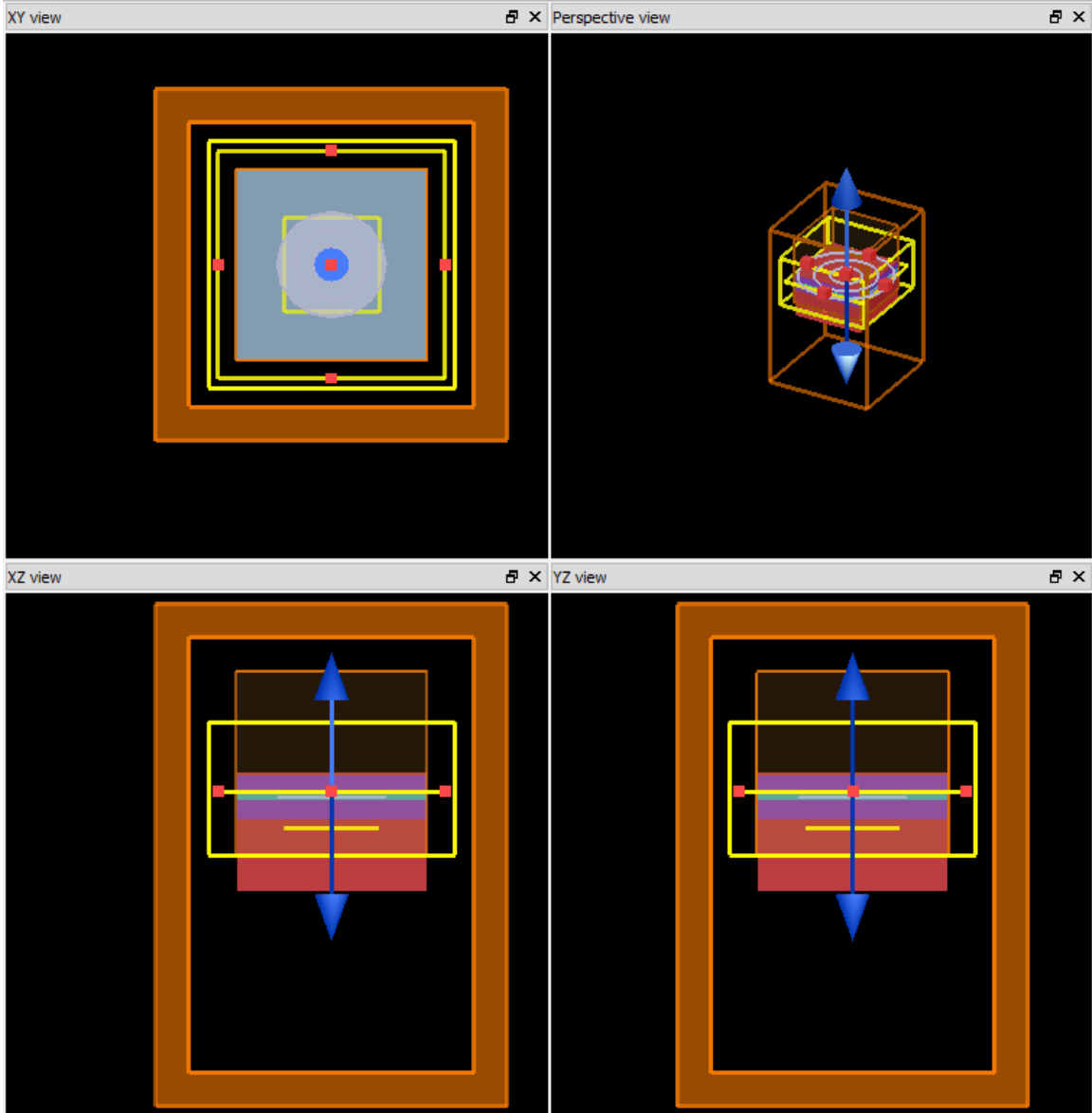


Figure 4.2 Schematic Illustration of AlInN-based Planar UV LED with TM Polarized Light Source.

4.3 Results

The simulation for estimation of LEE for Planar UV LED at 282nm was done and found to be 8% for TE polarized light source. But for TM polarized light it was found to be only 0.98%. This would clearly indicate the superiority of NW design with respect to LEE. The electric field profile is shown below in Figure 4.3. There is noticeable change in electric field intensity and TM field is less intense resulting in lower light extraction efficiency.

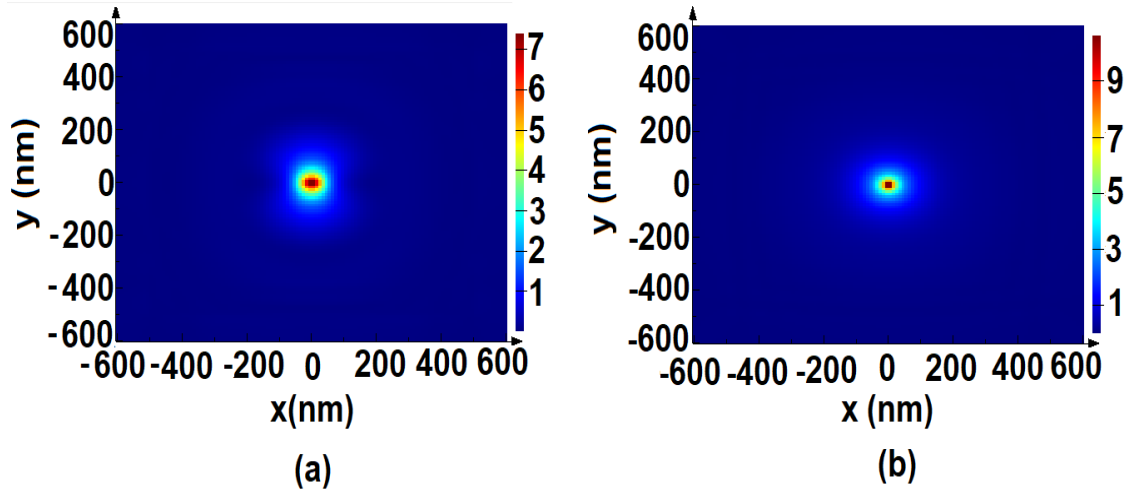


Figure 4.3 Cross-Sectional Near-Field Electric Field Intensity of a TM-Polarized Light Source in (a), and TE-Polarized Light Source in (b) for AlInN Planar LED.

Firstly, an investigation into the LEE of the studied NW LED structure for wavelength ranges from 220 nm to 400 nm was done. Both TE and TM-polarized light sources are examined here, and the results are presented in Figure 4.4. TM-polarized emission was found to be favored by this AlInN based NW structure, since the LEE for TM-polarized light source is found to be consistently higher than that of the TE-polarized light source for the entire range of wavelength in the UV region. It is already established that the height of the *p*-GaN should be minimized for the reduction in absorption of the UV Light [51]. TM-polarized emission, while only ~13% of LEE is obtained for TE-polarized emission. The passivation layer helps with the suppression of the surface recombination arising from surface states. The cavity effect leads to Photon trapping within the core and this must be considered while choosing NW passivation material [53]. So, a transparent material for the target range with a smaller refractive index is often used. For this study, HfO₂ was considered with an extinction coefficient (*k*) of 0.0045 [48].

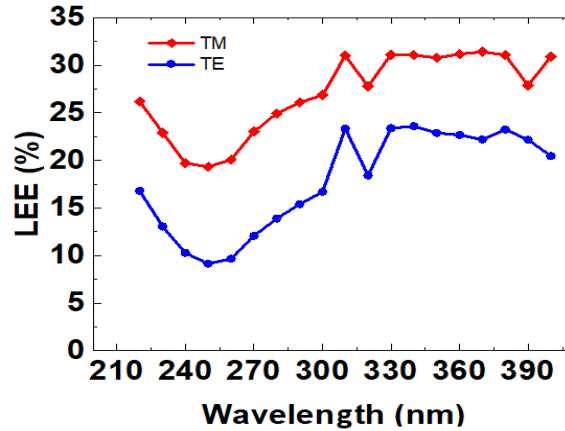


Figure 4.4 The LEE of the AlInN NW LED as a Function of Wavelength.

Source: M. Patel, B. Jain, R. T. Velpula, and H. P. T. Nguyen, "Effect of HfO₂ Passivation Layer on Light Extraction Efficiency of AlInN Nanowire Ultraviolet Light-Emitting Diodes." *ECS Transaction*, In Press.

As shown in Figure 4.2, for the 282 nm wavelength, ~25.2% of LEE can be achieved for Ideally, HfO₂ with a smaller refractive index than the NW core, which is about 2.4365, in the NW should suppress the cavity effect, which traps photons and reduce the total internal reflection for all passivation layer thickness consistently. Additionally, a lower absorption coefficient should lead to more photon extraction leading to a higher LEE.

The dependence of LEE for AlInN NW LED with both TM and TE polarized light sources with respect to various thicknesses of HfO₂ passivation layer ranging from 5 nm to 75nm is shown in Figure 4.5. The LEE due to TE-polarized light source is presented in Figure 4.5(b) while, the LEE due to TM-polarized light source is presented in Figure 4.5 (a). Although the critical parameters for the LEE are the refractive index and the absorption coefficient, it is understood that passivation layer thickness also influences the extraction of light through the NW sidewall. As shown in Figure 3, maximum LEE of ~ 40% for TM and ~ 32% for TE polarized light can be achieved for the AlInN NW LED with an HfO₂ passivation layer of 40 nm thickness. However, for the HfO₂ layer with a lower thickness than ~ 25 nm, LEE has a decreasing trend in both TE and TM polarized light sources as

the thin passivation layer properties only have a minor effect on the photon's extraction. A mirrored result for LEE, for a greater passivation thickness, is seen for the HfO_2 since it decreases as the thickness of the passivation layer is further increased to 75 nm thickness. This is due to enhanced total internal reflection and coupling of resonant modes between the NW core and the passivation layer. The emission of light from the sidewalls and the top surface of the AlInN NW for different HfO_2 passivation layer thickness is also studied and included in Figure 4.5, along with the total emitted LEE. It is found that most of the total emitted light is emitting from the sidewalls of the NWs in both the case of TE and TM polarized light sources.

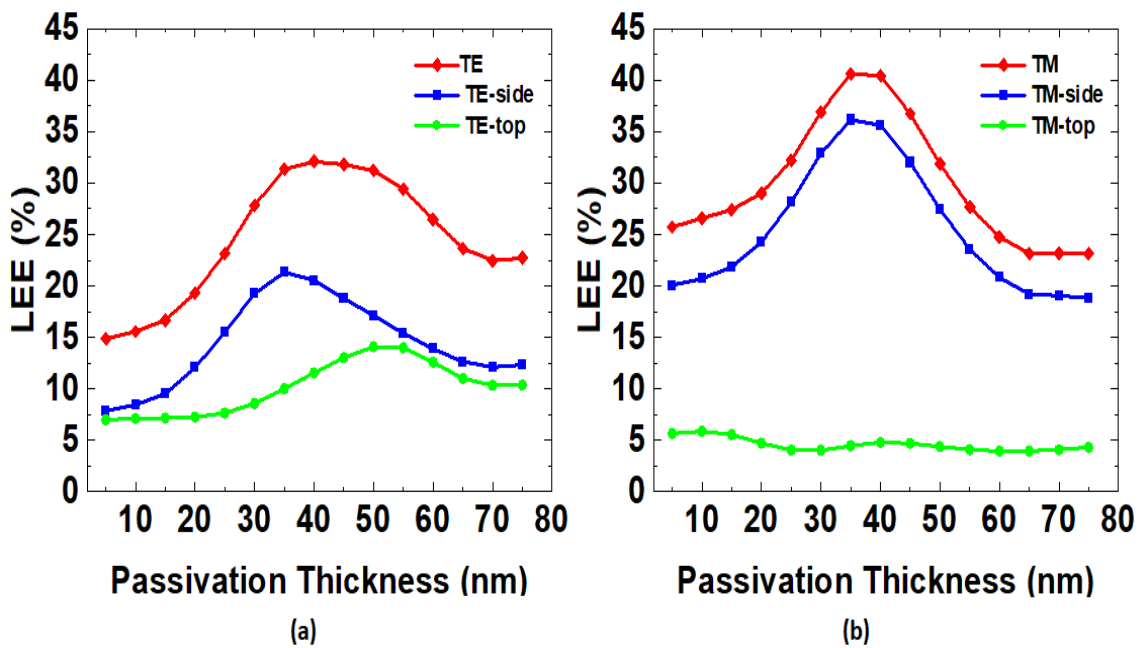


Figure 4.5 (a) TE-Polarized, (b) TM Polarized LEE of the AlInN NW LED as a Function of HfO_2 Passivation Layer Thickness.

Source: M. Patel, B. Jain, R. T. Velpula, and H. P. T. Nguyen, "Effect of HfO_2 Passivation Layer on Light Extraction Efficiency of AlInN Nanowire Ultraviolet Light-Emitting Diodes." *ECS Transaction*, In Press.

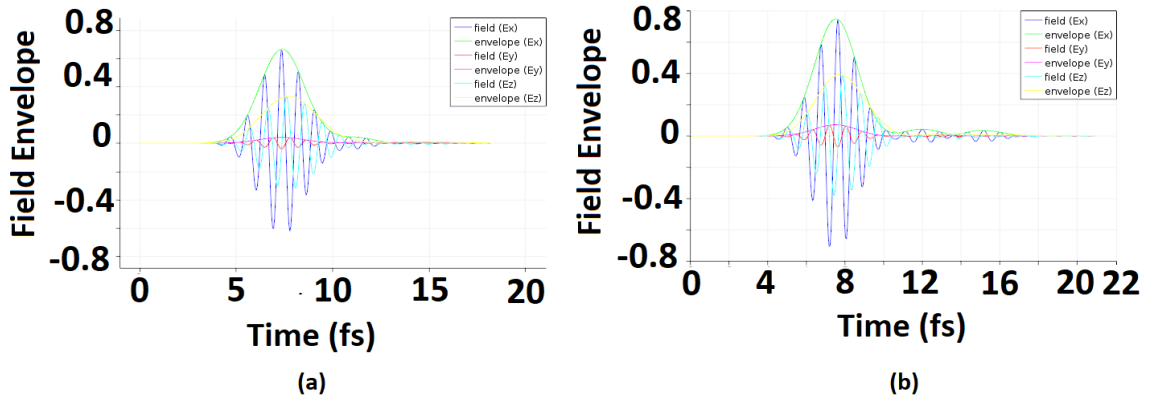


Figure 4.6 Electric Field Profile for a TM-Polarized Light Source for a AlInN NW Core in the X-Y Plane for (a) 40 nm Thick HfO₂ Passivation Layer, (b) 75 nm Thick HfO₂ Passivation Layer.

Source: M. Patel, B. Jain, R. T. Velpula, and H. P. T. Nguyen, "Effect of HfO₂ Passivation Layer on Light Extraction Efficiency of AlInN Nanowire Ultraviolet Light-Emitting Diodes." *ECS Transaction*, In Press.

The electric field vs. time plot for the NW core with 40 nm thick and 75 nm thick HfO₂ passivation layer is shown in Figure 4.6. This figure provides information regarding the decaying of the localized resonance in the NW core. The electric field resonance plot in Figure 4.4 clearly shows the enhanced localized resonance in the 75 nm thick passivation layer as compared to the 40 nm passivation layer. The observed enhancement of these resonance results from increased photon confinement, paired with an increased absorption in the passivation layer; thus, the extraction efficiency of the TM-polarized light drops at 75 nm thickness, as shown in Figure 4.5. The absorption plots for the passivation layer of thickness 40 nm and 75 nm are shown in Figure 4.7. The amount of absorption clearly reflected by an increase in intensity, as seen in Figure 4.7. Greater absorption in the core is resulted due to higher photon confinement, indicated by intensive red core as seen in Figure 4.7(b). Thus, an increased core absorption can be attributed to more prolonged and enhanced resonance, resulting in fewer photons escaping the NW core, contributing to decreased LEE.

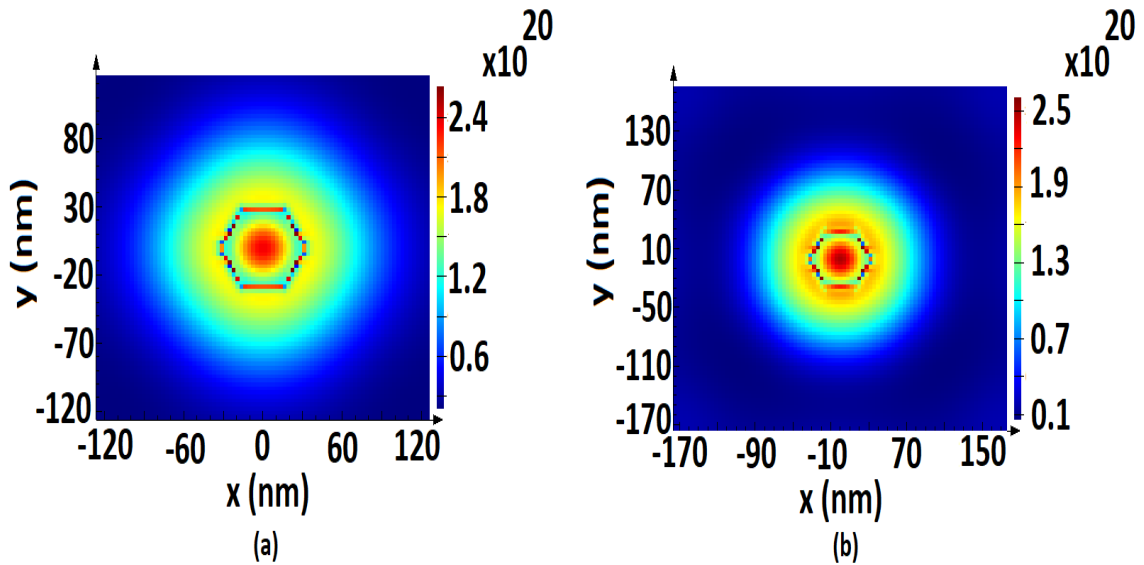


Figure 4.7 Cross-Sectional Absorption Profile in the X-Y Plane for (a) 40 nm Thick Passivation Layer, (b) 75 nm Passivation Layer.

Source: M. Patel, B. Jain, R. T. Velpula, and H. P. T. Nguyen, "Effect of HfO_2 Passivation Layer on Light Extraction Efficiency of AlInN Nanowire Ultraviolet Light-Emitting Diodes." *ECS Transaction*, In Press.

Figure 4.8 can be used to further understand the effect of passivation layer thickness on the TM-polarized light extraction, the electric field intensity distribution of NW LED with non-passivated, 40 nm, 75 nm thick HfO_2 passivation layer. As clearly illustrated in the electric field intensity plots, the TM-polarized photons, which are primarily concentrated near the active region, can easily penetrate through the NW with a thin HfO_2 passivation layer and resulting in increasing LEE. However, compared to NW with a 40 nm passivation layer, the electric field intensity is poor in the case of NW without passivation layer and NW with a 75 nm passivation layer. Photons trapping along the NW core is severe due to the enhancement of resonant modes inside the thick passivation layer as the thickness of passivation layer increases beyond 40 nm.

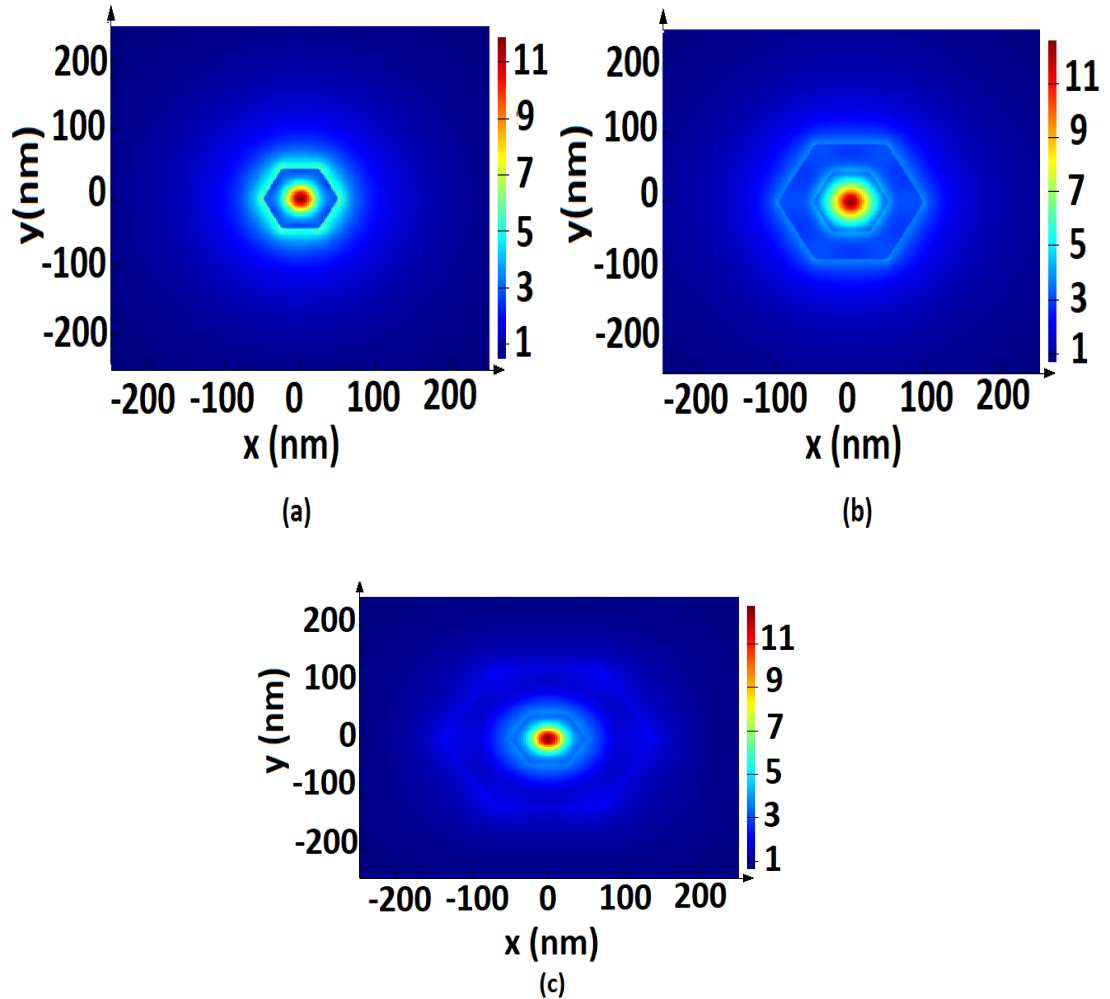


Figure 4.8 Cross-Sectional Near-Field Electric Field Intensity of a TM-Polarized Light Source for AlInN NW LED (a) Without Passivation Layer, (b) With 40 nm Passivation Layer, and (c) 75 nm Passivation Layer for TM-Polarized Light Source in the X-Y Plane.

Source: M. Patel, B. Jain, R. T. Velpula, and H. P. T. Nguyen, "Effect of HfO₂ Passivation Layer on Light Extraction Efficiency of AlInN Nanowire Ultraviolet Light-Emitting Diodes." *ECS Transaction*, In Press.

From this analysis, a variation of LEE was observed with a different passivation layer thickness. The use of HfO₂ as a passivation layer has a smaller refractive index than the NW active region, results in better light extraction compared to NW without passivation. The maximum achievable TM and TE-polarized LEE is ~40.6% and 32% using 40 nm HfO₂ passivated structure at ~282 nm wavelength.

CHAPTER 5

CONCLUSION AND FUTURE WORK

From the above results we can make some sense for the effectiveness of the methods described in the above chapters. From our investigation of the unique concave QB based AlGa_N UV LEDs the numerical results show that the introduction of the proposed QBs is favorable for achieving an enhanced output optical power due to lower electron mean free path and velocity. This helps to show promising efficient deep AlGa_N UV light emitters for fabrication and further experimentation.

Further, the use of HfO₂ as a passivation layer has a smaller refractive index than the nanowire (NW) active region, resulting in larger light extraction compared to NW without passivation. The maximum achievable TM and TE-polarized LEE is ~40.6% and 32% using 40 nm HfO₂ passivated structure at ~282 nm wavelength. Future work to address the impact of various photonic crystal designs within an array of NWs, such as uniformity in NW diameter, height, spacing, and peak emission wavelength, and QW position, is required to provide more comprehensive modeling of the NW LED Performance. Additionally, the *p*-type doping has height activation energy for AlInN material system with Magnesium as dopant atom so this needs to be addressed as well. So, these topics are briefly discussed below and are important future study needed.

5.1 Study of Doping and Defects in AlInN UV LEDs.

With given reasons in chapter 4, exploration of AlInN UV LED is necessary and is an important material candidate for high-power electronics and deep ultraviolet light sources. The realization of AlInN devices with ideal optical and electronic properties requires strict control over doping and an understanding of the microscopic origin of these properties.

Additionally, obtaining high p type conductivity in nitrides is found to be difficult resulting in an impeded development of the AlInN based devices similar to other nitride devices. Even with considerable efforts the challenge of *p*-type doping is ongoing. Additionally, the lack of a reliable method to analyze the properties of the acceptor levels makes p doping in nitrides more difficult [54]. Within various approaches, co-doping has been viewed as an important strategy [55]. Candidate co-dopants need to be studied for its effectiveness, so a theoretical study is important before fabrication. This can be achieved using Density Functional Theory (DFT).

The many-body Schrodinger equation is the fundamental equation used to describe a system made crystal lattice of ions, a non-relativistic electron in an arbitrary potential, but this many-body Schrodinger equation is intractable to solve for many material systems with current computing availability. So, using, Kohn and Sham method/equation [56] where they used the Hohenberg-Kohn theorem to derive an expression where electron-electron interactions are replaced by an interaction between the single-electron orbitals and an effective potential. Also, the electron densities of the many-electron and single-electron systems are proven to be identical with an appropriate effective potential, with these identical electron densities, the Hohenberg-Kohn theorem [57] implies that the ground-state energies will be the same, forming the basis for DFT. DFT calculations can be performed using the Quantum Espresso Package, an open-source software.

Quantum Espresso is a popular electronic structure code because of its speed and reliable pseudopotential library. Pseudopotentials replace core electron with an effective screened potential around the nucleus since the electrons in orbitals are rapidly oscillating resulting in slow convergence. A basic calibration study was done to see the effectiveness

of co-doping in GaN, with an intent to use similar method for AlInN, based on previous reported work. In a $2 \times 2 \times 2$ supercell, two Ga atoms are substituted by In and Mg randomly and a generalized gradient approximation of Perdew-Burke-Ernzerhof functionals as the exchange correlation potential is used for the simulation. The doped supercell is shown below with the calculated Density of state indicating modulation effect of orbital coupling between doping atoms and the pure GaN. The upward shift of the valence band maximum is expected to facilitate ionization of acceptors.

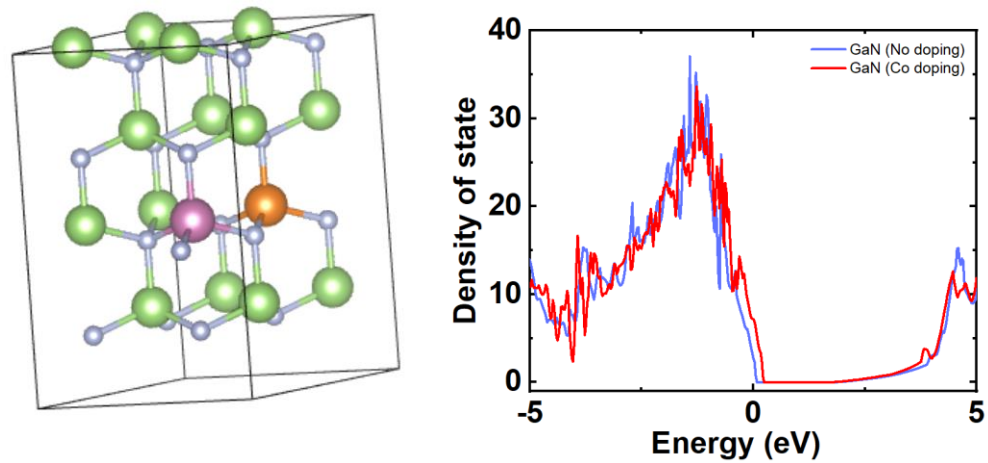


Figure 5.1 Doped GaN and its Effect on Density of State for GaN Material.

The optical and electronic properties of a semiconductor are majorly dependent upon the populations of point defects in the material. Point defects are local irregularities in the crystal structure with limited spatial extent in any dimension by possessing a missing host atom, or a host atom which has been replaced by an atom of a different element. By introducing electronic states inside the bandgap, the point defects control electronic properties thus changing the energy required to promote electrons into the conduction band or holes into the valence band giving rise to variance in a fabricated structure. This make

it critical to study point defects and its formation energy to mitigate it, but it is usually difficult to use experimental methods in contrast suitable for simulation study method.

5.2 Study of Photonic Crystal Structure based AlInN UV NW LEDs.

Firstly, the performance of photonic crystal structure NW LEDs can easily compete with standard LEDs already since it addresses the problem of total internal reflection, which is commonly a major issue in volume emitters or thin-film LEDs. Photonic crystal structure offers advantages beyond the pure extraction enhancement. It combines the effectiveness of a NW structure with the intrinsic influence of photonic crystal structure on the dispersion relation of light, i.e., band folding due to Bloch's theorem. Due to their periodicity, it is possible to shape the emission profile of a LED [58]. This could be of great advantage for applications based on broad anti-microbial action since it can compete with traditional UV lamps. Due to superior optical mode control the Photonic crystal structures can efficiently couple guided modes out of the LEDs [59]. Luminescence emission intensity and stability can be enhanced significantly with precise control of the NW physical properties like radius, spacing between each NW, etc. through selective area epitaxy, [60-62]. An example structure is shown in Figure 5.2.

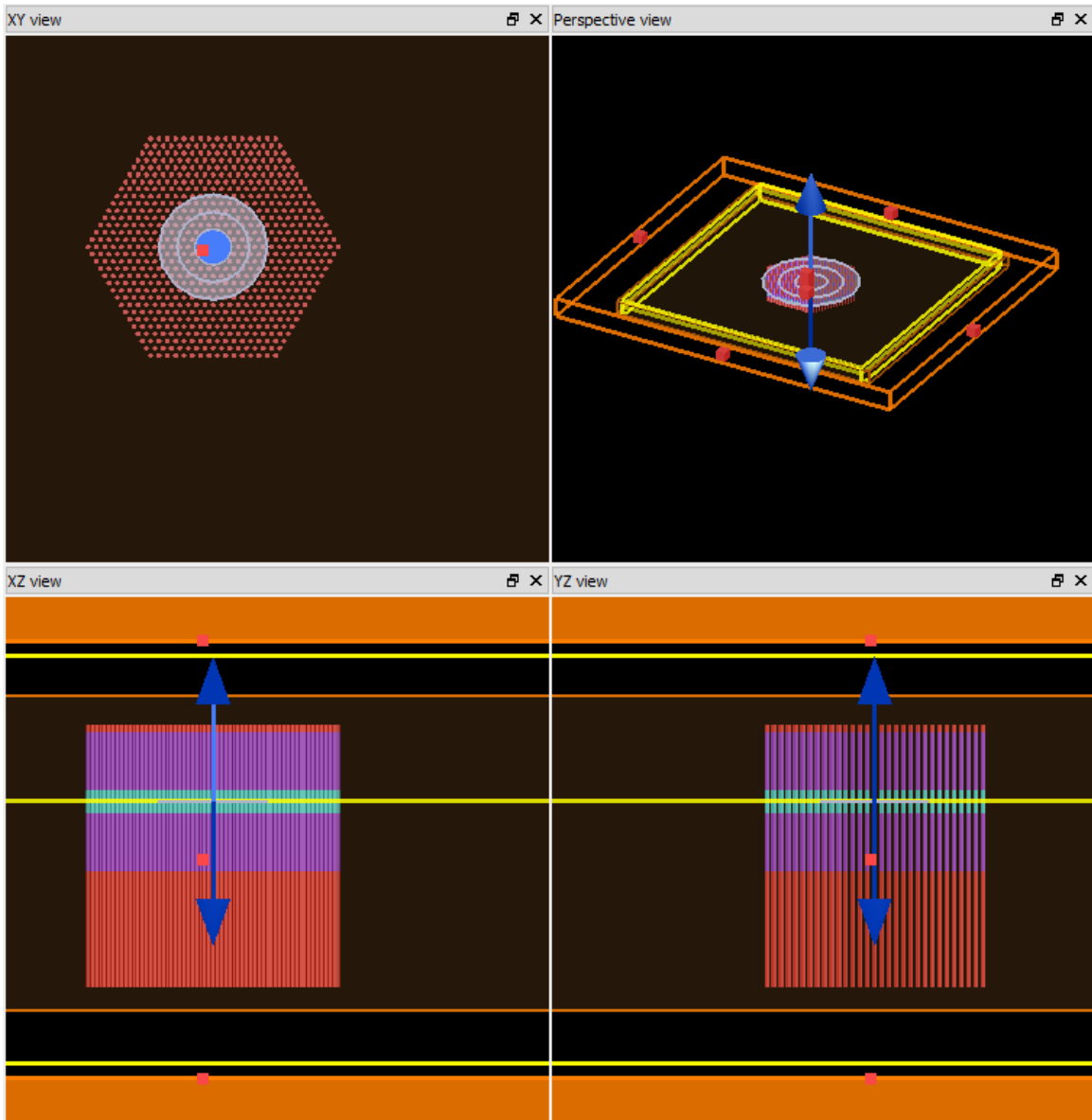


Figure 5.2 Example for Photonic Crystal Structure of an AlInN NW UV-LED.

BIBLIOGRAPHY

1. L. Endres, and R. Breit, "UV Radiation, Irradiation, Dosimetry. In: Krutmann J., Hönigsmann H., Elmetts C.A., Bergstresser P.R. (eds)", *Dermatological Phototherapy and Photodiagnostic Methods*, Springer: Berlin (2001).
2. M. Vázquez, and A. Hanslmeier, "Historical Introduction. In: Ultraviolet Radiation in the Solar System", *Astrophysics and Space Science Library*, **331**, Springer: Dordrecht (2006).
3. D.A. Sarigiannis, S.P. Karakitsios, M.P. Antonakopoulou, and A. Gotti, "Exposure analysis of accidental release of mercury from compact fluorescent lamps (CFLs)", *Science of the Total Environment*, 435–436:306-315 (2012).
4. H. Unlu, H. Morkoç, and G. Ji, "Principles and Technology of MODFETs", *United Kingdom: Wiley* (1991).
5. K. Yee, "Numerical solution of initial boundary value problems involving maxwell's equations in isotropic media," *IEEE Transactions on Antennas and Propagation*, **14**, pp. 302-307, (1966).
6. Lumerical Inc. <https://www.lumerical.com>.
7. S. S. Li, "Semiconductor physical electronics", *Springer Science & Business Media* (2012).
8. W. T. Shockley, and W. T. Read Jr, "Statistics of the recombinations of holes and electrons", *Physical Review*, **87**(5), 835 (1952).
9. M. H. Kim, M. F. Schubert, Q. Dai, J. K. Kim, E. F. Schubert, J. Piprek, and Y. Park, "Origin of efficiency droop in GaN-based light-emitting diodes", *Applied Physics Letters*, **91**, 183507 (2007).
10. APSYS, "Crosslight technical manuals", *Crosslight Software Inc.*, Burnaby, Canada (2010).
11. J. Piprek, "Nitride Semiconductor Devices: Principles and Simulation", *Wiley*, **590** (2007),
12. C. Coughlan, S. Schulz, M. A. Caro, and E. P. O'Reilly, "Band gap bowing and optical polarization switching in AlGaIn alloys", *Physica Status Solidi B*, **252**, 879–884 (2015).
13. S. Chuang and C. Chang, "*k*·*p* method for strained wurtzite semiconductors", *Physical Review B*, **54**, 2491 (1996).
14. J. Yun, J.I. Shim, and H. Hirayama, "Analysis of efficiency droop in 280-nm AlGaIn multiple-quantum-well light-emitting diodes based on carrier rate equation," *Applied Physics Express*, **8**, 022104 (2015).
15. K. Nam, M. Nakarmi, J. Li, J. Lin, and H. Jiang, "Mg acceptor level in AlN probed by deep ultraviolet photoluminescence," *Applied Physics Letters*, **83**, 878–880 (2003).
16. M. Nakarmi, N. Nepal, J. Lin, and H. Jiang, "Photoluminescence studies of impurity transitions in Mg-doped AlGaIn alloys", *Applied Physics Letters*, **94**, 091903 (2009).
17. R. Collazo, S. Mita, J. Xie, A. Rice, J. Tweedie, R. Dalmau, and Z. Sitar, "Progress on n-type doping of AlGaIn alloys on AlN single crystal substrates for UV optoelectronic applications", *Physica Status Solidi C*, **8**, 2031–2033 (2011).

18. V. Fiorentini, F. Bernardini, and O. Ambacher, "Evidence for nonlinear macroscopic polarization in III–V nitride alloy heterostructures", *Applied Physics Letters*, **80**, 1204–1206 (2002).
19. J. Lang, F. Xu, W. Ge, B. Liu, N. Zhang, Y. Sun, J. Wang, M. Wang, N. Xie, and X. Fang, "Greatly enhanced performance of AlGaIn-based deep ultraviolet light emitting diodes by introducing a polarization modulated electron blocking layer", *Optical Express*, **27**, A1458-A1466 (2019).
20. B. So, J. Kim, E. Shin, T. Kwak, T. Kim, and O. Nam, "Efficiency Improvement of Deep-Ultraviolet Light Emitting Diodes with Gradient Electron Blocking Layers", *Physica Status Solidi A*, **215**, 1700677 (2018).
21. B. Jain, R. T. Velpula, S. Velpula, H.D. Nguyen, and H. P. T. Nguyen, "Enhanced hole transport in AlGaIn deep ultraviolet light-emitting diodes using a double-sided step graded superlattice electron blocking layer", *Journal of the Optical Society of America B : Optical Physics*, **37**, 2564-2569 (2020).
22. B. So, J. Kim, T. Kwak, T. Kim, J. Lee, U. Choi, and O. Nam, "Improved carrier injection of AlGaIn-based deep ultraviolet light emitting diodes with graded superlattice electron blocking layers", *Royal Society of Chemistry Advances*, **8**, 35528-35533 (2018).
23. Y.K. Kuo, F.-M. Chen, B.C. Lin, J.Y. Chang, Y.H. Shih, and H.C. Kuo, "Simulation and experimental study on barrier thickness of superlattice electron blocking layer in near-ultraviolet light-emitting diodes" *IEEE Journal of Quantum Electronics*, **52**, 1-6 (2016).
24. N. Maeda and H. Hirayama, "Realization of high-efficiency deep-UV LEDs using transparent p-AlGaIn contact layer", *Physica Status Solidi C*, **10**, 1521-1524 (2013).
25. R. T. Velpula, B. Jain, S. Velpula, H.-D. Nguyen, and H. P. T. Nguyen, "High-performance electron-blocking-layer-free deep ultraviolet light-emitting diodes implementing a strip-in-a-barrier structure", *Optics Letters*, **45**, 5125-5128 (2020).
26. L. He, W. Zhao, K. Zhang, C. He, H. Wu, N. Liu, W. Song, Z. Chen, and S. Li, "Performance enhancement of AlGaIn-based 365 nm ultraviolet light-emitting diodes with a band-engineering last quantum barrier", *Optics Letters*, **43**, 515-518 (2018).
27. R. T. Velpula, B. Jain, H. Q. T. Bui, F. M. Shakiba, J. Jude, M. Tumuna, H.D. Nguyen, T. R. Lenka, and H. P. T. Nguyen, "Improving carrier transport in AlGaIn deep-ultraviolet light-emitting diodes using a strip-in-a-barrier structure," *Applied Optics*, **59**, 5276-5281 (2020).
28. Yan, J. Wang, Y. Zhang, P. Cong, L. Sun, Y. Tian, C. Zhao, and J. Li, "AlGaIn-based deep-ultraviolet light-emitting diodes grown on high-quality AlN template using MOVPE", *Journal of Crystal Growth*, **414**, 254-257 (2015).
29. Y. P. Varshni, "Temperature dependence of the energy gap in semiconductors", *Physica*, **34**, 149-154 (1967).
30. B. Jain, R. T. Velpula, M. Patel, and H.P.T. Nguyen, Controlled carrier mean free path for the enhanced efficiency of III-nitride deep-ultraviolet light-emitting diodes." *Applied Optics* **60**, **11**, 3088-3093, (2021).

31. I. Vurgaftman and J. N. Meyer, "Band parameters for nitrogen-containing semiconductors", *Journal of Applied Physics*, **94**, 3675-3696 (2003).
32. J. Yan, J. Wang, Y. Zhang, P. Cong, L. Sun, Y. Tian, C. Zhao, and J. Li, "AlGaIn-based deep-ultraviolet light-emitting diodes grown on high-quality AlN template using MOVPE", *Journal of Crystal Growth*, **414**, 254-257 (2015).
33. X. Zhang, T. Taliercio, S. Kolliakos, and P. Lefebvre, "Influence of electron-phonon interaction on the optical properties of III nitride semiconductors", *Journal of Physics: Condensed Matter*, **13**, 7053 (2001).
34. M. Kuball, "Raman spectroscopy of GaN, AlGaIn and AlN for process and growth monitoring/control," *Surface and Interface Analysis*, **31**, 987-999 (2001).
35. M. Mora-Ramos and L. Gaggero-Sager, "Electron-optical-phonon scattering rates in AlGaIn/GaN-based single heterostructures", *Physica Status Solidi C*, **2**, 3002-3005 (2005).
36. B. Jain, R. T. Velpula, H. Q. T. Bui, H.D. Nguyen, T. R. Lenka, T. K. Nguyen, and H. P. T. Nguyen, "High performance electron blocking layer-free InGaIn/GaN nanowire white-light-emitting diodes", *Optical Express*, **28**, 665-675 (2020).
37. Y. A. Yin, N. Wang, G. Fan, and Y. Zhang, "Investigation of AlGaIn-based deep-ultraviolet light-emitting diodes with composition-varying AlGaIn multilayer barriers", *Superlattices and Microstructures*, **76**, 149-155 (2014).
38. Z.H. Zhang, W. Liu, Z. Ju, S.T. Tan, Y. Ji, Z. Kyaw, X. Zhang, L. Wang, X. Wei Sun, and H. Volkan Demir, "Self-screening of the quantum confined Stark effect by the polarization induced bulk charges in the quantum barriers", *Applied Physics Letters*, **104**, 243501 (2014).
39. C. Zhao, T.K. Ng, A. Prabaswara, M. Conroy, S. Jahangir, T. Frost, J. O'Connell, J.D. Holmes, P.J. Parbrook, P. Bhattacharya, and B.S. Ooi, "An enhanced surface passivation effect in InGaIn/GaN disk-in-nanowire light emitting diodes for mitigating Shockley-Read-Hall recombination", *Nanoscale*, **7**, 16658 (2015).
40. A. Armstrong, Q. Li, Y. Lin, A. A. Talin, and G. T. Wang, "GaN nanowire surface state observed using deep level optical spectroscopy," *Applied Physics Letters*, **96**, 163106 (2010).
41. E. Schubert, "Light-Emitting Diodes", *Cambridge: Cambridge University*, (2nd ed.) (2006).
42. K. Nam, J. Li, M. Nakarmi, J. Lin, and H. Jiang. "Unique optical properties of AlGaIn alloys and related ultraviolet emitters", *Applied Physics Letters*, **84**, 5264 (2004).
43. M. Kneissl, T.Y. Seong, J. Han, and H. Amano, "The emergence and prospects of deep-ultraviolet light-emitting diode technologies", *Nature Photonics*, **13**, 233 (2019).
44. P. Zhu, "Frustrated total internal reflection in organic light-emitting diodes employing sphere cavity embedded in polystyrene", *Journal of Optics*, **18**, 025403 (2016).
45. S. D. Gedney, "An anisotropic perfectly matched layer-absorbing medium for the truncation of FDTD lattices", *IEEE transactions on Antennas and Propagation*, **44**, 1630 (1996).
46. E. D. Palik, "Handbook of optical constants of solids", *Academic Press* (1998).
47. S. Adachi, "Handbook on Optical Constants of Semiconductors: In Tables And Figures", *World Scientific* (2012).

48. J.M. Khoshman, and M.E. Kordesch, "Optical properties of a-HfO₂ thin films", *Surface and Coatings Technology*, **201**, 3530 (2006).
49. H.Y. Ryu, "Large enhancement of light extraction efficiency in AlGa_N-based nanorod ultraviolet light-emitting diode structures", *Nanoscale research letters*, **9**, 58 (2014).
50. A.L. Henneghien, B. Gayral, Y. Desieres, and J.M. Gerard, "Simulation of waveguiding and emitting properties of semiconductor nanowires with hexagonal or circular sections", *Journal of the Optical Society of America. B*, **26**, 2396 (2009).
51. H.Y. Ryu, I.G. Choi, H.S. Choi, and J.I. Shim, "Investigation of light extraction efficiency in AlGa_N deep-ultraviolet light-emitting diodes", *Applied Physics Express*, **6**, 062101 (2013).
52. M. Patel, B. Jain, R. T. Velpula, and H. P. T. Nguyen, "Effect of HfO₂ Passivation Layer on Light Extraction Efficiency of AlInN Nanowire Ultraviolet Light-Emitting Diodes." In *239th ECS Meeting with the 18th International Meeting on Chemical Sensors (IMCS)(May 30-June 3, 2021)*. ECS (2021).
53. Y.K. Ooi, C. Liu, and J. Zhang, "Analysis of polarization-dependent light extraction and effect of passivation layer for 230-nm AlGa_N nanowire light-emitting diodes", *IEEE Photonics Journal*, **9**, 1 (2017).
54. Z. Liu, Y. Huang, X. Yi, B. Fu, G. Yuan, J. Wang, J. Li, and Y. Zhang, *Scientific Reports*, **6**, 32033 (2016).
55. Y. Aoyagi, M. Takeuchi, S. Iwai and H. Hirayama, *Applied Physics Letters*, **99**, 112110 (2011).
56. W. Kohn, and L.J. Sham, *Physical Review A*, **140**, p. 1133 (1964).
57. P. Hohenberg, and W. Kohn, *Physical Review B*, **136**, p. 864 (1964).
58. J. J. Wierer, M. R. Krames, J. E. Epler, N. F. Gardner, M.G. Craford, J. R. Wendt, J. A. Simmons, and M. M. Sigalas, "InGa_N/Ga_N quantum-well heterostructure light-emitting diodes employing photonic crystal structures", *Applied Physics Letters*, **84**, 3885 (2004).
59. J. J. Wierer, A. David, and M. M. Megens, "III-nitride photonic-crystal light-emitting diodes with high extraction efficiency", *Nature Photonics*, **3**, 163–169 (2009).
60. M. Djavid and Z. Mi, "Enhancing the light extraction efficiency of AlGa_N deep ultraviolet light emitting diodes by using nanowire structures", *Applied Physics Letters*, **108** (5), 051102 (2016).
61. Y. H. Ra, R. T. Rashid, X. Liu, J. Lee, and Z. Mi, "Scalable nanowire photonic crystals: Molding the light emission of InGa_N", *Advanced Functional Materials*, **27**(38), 1702364 (2017).
62. P. Du, L. Rao, Y. Liu, and Z. Cheng, "Enhancing the light extraction efficiency of AlGa_N LED with nanowire photonic crystal and graphene transparent electrode", *Superlattices and Microstructures*, **133**, 106216 (2019).